Simulation of the direct and semidirect aerosol effects on the southern Africa regional climate during the biomass burning season

F. Tummon, F. Solmon, C. Liousse, M. Tadross

To cite this version:

F. Tummon, F. Solmon, C. Liousse, M. Tadross. Simulation of the direct and semidirect aerosol effects on the southern Africa regional climate during the biomass burning season. Journal of Geophysical Research: Atmospheres, 2010, 115, pp.D19206. 10.1029/2009JD013738. hal-00563632

HAL Id: hal-00563632
https://hal.science/hal-00563632v1

Submitted on 25 Jun 2022

JOURNAL OF GEOPHYSICAL RESEARCH, VOL. 115, D19206, doi:10.1029/2009JD013738, 2010

Simulation of the direct and semidirect aerosol effects on the southern Africa regional climate during the biomass burning season

F. Tummon,[1,2] F. Solmon,[1,3] C. Liousse,[1] and M. Tadross[2]

Received 22 December 2009; revised 8 April 2010; accepted 7 June 2010; published 7 October 2010.

[1] The regional climate model RegCM3 was used to simulate the direct and semidirect radiative effects of biomass burning and dust aerosol over southern Africa during the austral winter season. Simulated aerosols were found to induce changes in the regional surface fluxes and atmospheric dynamics. Clear-sky surface radiative forcing decreased by up to −60 W/m^2 in the main biomass burning region, resulting in decreased surface turbulent fluxes and PBL height as well as reduced surface temperatures. The positive temperature bias over the western half of the subcontinent was thus reduced. Radiative absorption by biomass burning aerosols resulted in diabatic warming of the atmosphere, peaking near 700 hPa at a rate of up to 1°C/d. Simulated surface cooling and heating at altitude stabilized the lower troposphere below 700 hPa. Above 700 hPa, stability was reduced in the equatorial region between 5°N and 5°S through an elevated heat pump mechanism, enhancing deep convection and precipitation. The southern branch of the African Easterly Jet was enhanced and shifted southward, likely as a result of the changes in the surface temperature gradient induced by both the reduction in solar radiation reaching the surface and through precipitation-induced surface cooling in the equatorial region. Daily-scale aerosol outflow events to the southwest Indian Ocean were also investigated, these events occurring with the passage of a westerly wave. It was found that the aerosol loading enhanced baroclinicity along the leading edge of the frontal system, thus intensifying and narrowing the band of precipitation in this zone.

Citation: Tummon, F., F. Solmon, C. Liousse, and M. Tadross (2010), Simulation of the direct and semidirect aerosol effects on the southern Africa regional climate during the biomass burning season, *J. Geophys. Res.*, *115*, D19206, doi:10.1029/2009JD013738.

1. Introduction

[2] Approximately 80% of all global biomass burning occurs in the tropical regions [*Keil and Haywood*, 2003], with approximately 440 million hectares of land exposed to fire annually [*Scholes and Andeae*, 2000]. Some of the most extensive burning occurs on the African continent, where an estimated one third of total global pyrogenic emissions are produced [*Alleaume et al.*, 2005]. Biomass burning activity in southern Africa progresses from north to south during the dry, austral winter, beginning in June, peaking in July and August and then decreasing in intensity until late October when the season comes to an end [*Cahoon et al.*, 1992; *Maenhaut et al.*, 1996; *Liousse et al.*, 1996; *Swap et al.*, 1996]. Although domestic fuel is widely used for heating and cooking purposes, particularly in winter, the largest source of biomass burning material in southern Africa is savanna vegetation [*Swap et al.*, 2002, 2003]. As a result of highly seasonal rainfall, fuel accumulated during the wet season becomes dry and prone to burning during the dry season. Added to this, is the fact that the regional savanna vegetation is generally not very palatable; therefore, grazing is reduced, further contributing to the accumulation of biomass [*Scholes and Andeae*, 2000]. Biomass burning is carried out largely as part of regional agricultural practices [*Maenhaut et al.*, 1996; *Eck et al.*, 2003] and between 70% and 90% of all fires are believed to be of anthropogenic origin [*Helas and Pienaar*, 1996].

[3] Biomass burning alters regional aerosol and trace gas composition [*Crutzen et al.*, 1979; *Seiler and Crutzen*, 1980; *Crutzen and Andreae*, 1990; *Andreae and Merlet*, 2001], and impacts atmospheric chemistry, radiative balance and biogeochemical cycles [e.g., *Liousse et al.*, 1996; *Garstang et al.*, 1998; *Dubovik et al.*, 2000; *Tyson and Gatebe*, 2001; *Kaufman et al.*, 2002; *Takemura et al.*, 2002]. Aerosols from vegetation fires consist predominantly of fine organic particles in combination with various other products, most notably, black carbon [*Kaufman et al.*, 2002; *Posfai et al.*, 2003]. The percentage of black carbon emitted depends on the burning efficiency of the fire, with flaming fires producing a

---

[1] Laboratoire d'Aérologie, CNRS UMR5560, Université Paul Sabatier, Toulouse, France.

[2] Climate Systems Analysis Group, University of Cape Town, Cape Town, South Africa.

[3] Now at Abdus Salam International Centre for Theoretical Physics, Trieste, Italy.

0148-0227/10/2009JD013738

higher percentage of black carbon than smoldering fires [*Kaufman et al.*, 2002; *Posfai et al.*, 2003]. Also, as smoke particles age, progressively more black carbon particles become aggregated with organic and sulfate particles [*Posfai et al.*, 2003], potentially further enhancing the absorption efficiency of the black carbon (since the scattering coating may act as a lens, focusing more sunlight onto the dark core) [*Bergstrom et al.*, 1982; *Martins et al.*, 1998; *Kaufman et al.*, 2002; *Mikhailov et al.*, 2006; *Bond et al.*, 2006]. Estimating the absorption of solar radiation by biomass burning aerosols, particularly by black carbon, is vital in order to quantify their climatic impact. It has been estimated that in terms of global direct radiative forcing, the impact of black carbon alone exceeds that due to methane and may be second only to CO_2 [*Jacobson*, 2001; *Hansen et al.*, 1981]. Regionally, this forcing may be even larger.

[4] A number of field campaigns have been carried out characterizing the southern Africa regional aerosol burden, including the Southern Africa Fire-Atmosphere Research Initiative (SAFARI-92) [*Lindesay et al.*, 1996], the Southern Africa Atmosphere Research Initiative (SA'ARI) [*Helas et al.*, 1995], the Ben MacDhui High-Altitude Trace Gas and Aerosol Transport Experiment (BHATTEX) [*Piketh et al.*, 1999a], Aerosol Recirculation and Rainfall Experiment (ARREX) [*Terblanche et al.*, 2000], and the Southern African Fire Research Initiative (SAFARI-2000) [*Swap et al.*, 2003], as well as continuous ground-based observations through the AERONET [*Holben et al.*, 1998] and IDAF (http://medias.obs-mip.fr/Idaf/) networks.

[5] Results from these experimental campaigns and numerous other studies have shown that very stable atmospheric conditions prevail over southern Africa during the dry austral winter, which coincides with the main biomass burning season. Biomass burning products contribute significantly to the aerosol loading between 10°S and 20°S, where the highest fire counts are observed [*Piketh et al.*, 1999b]. As a result of the remarkable atmospheric stability, there is little cloud or rainfall over much of the region and absolutely stable layers form, persisting for up to 3 weeks at a time [*Tyson et al.*, 1996; *Scholes and Andeae*, 2000]. The general anticyclonic nature of atmospheric circulation over the region, which results in the formation of these stable layers, means that recirculation of aerosols and trace gases takes place to a significant extent, on local, regional, and subcontinental scales [*Torres et al.*, 2002]. On average over the year, up to 54% of air is recirculated at least once before exiting from the continent to either the Indian or Atlantic Ocean [*Tyson et al.*, 1996], and as a result, aerosol residence times over southern Africa are considerably longer than in other regions [*Freiman and Piketh*, 2003; *Liousse et al.*, 2004]. Long aerosol atmospheric residence times have implications for climate, particularly since well-aged biomass burning particles are more radiatively important [*Hobbs et al.*, 2003]. Studies using observations from the SAFARI-2000 campaign estimated surface radiative forcing of between −50 and −200 W/m^2 [e.g., *Campbell et al.*, 2003; *Bergstrom et al.*, 2003]. It has been suggested that the recirculating aerosol flux over southern Africa likely has a significant impact on regional climate, possibly causing surface cooling that may counteract projected surface warming [*Tyson et al.*, 1996], as well as potentially increasing atmospheric stability and inducing changes in circulation and precipitation patterns. To date, few modeling studies have investigated the regional climatic impacts of the aerosol burden over southern Africa. Those that have been carried out have used either global climate or aerosol models (with some focus on southern Africa) or radiative transfer models [e.g., *Myhre et al.*, 2003; *Abel et al.*, 2005; *Myhre et al.*, 2008].

[6] In order to attempt to quantify the regional climatic impacts of direct and semidirect aerosol radiative effects over southern Africa the International Centre for Theoretical Physics (ICTP) regional climate model RegCM3 is used in combination with a high temporal and spatial resolution biomass burning emissions inventory developed at the Laboratoire d'Aérologie, Toulouse, France [*Liousse et al.*, 2010]. The model, simulation design and emissions inventories used are described in section 2, while section 3 describes model validation. Section 4 evaluates and discusses the simulated regional aerosol-climate impacts as well as results from the two sensitivity tests carried out (one using the GFEDv2 emissions inventory [*Van der Werf et al.*, 2006] and a second using an adjustment to the sea surface temperature to account for aerosol feedback over the oceans). Lastly, some conclusions are given in section 5.

2. Model Description and Experiment Design

2.1. Model Description

[7] The dynamical core of RegCM3 is derived from the U. S. National Center for Atmospheric Research (NCAR)/ Penn State University mesoscale model 5 (MM5) [*Grell et al.*, 1994] and is designed specifically for climate time-scale simulations. It is a hydrostatic, sigma vertical coordinate, grid point-limited model with compressibility. The Biosphere-Atmosphere Transfer Scheme (BATS) [*Dickinson et al.*, 1993] is used to represent surface processes, while boundary layer physics are based on the nonlocal scheme of *Holtslag et al.* [1990]. Resolvable scale precipitation is explicitly calculated using the simplified moisture scheme of *Giorgi and Shields* [1999], updated by *Pal et al.* [2007]. The Grell scheme [*Grell*, 1993] with Fritsch-Chappell Closure [*Fritsch and Chappell*, 1980] is used to represent convective precipitation in our simulations. This convection scheme has been used in other RegCM3 studies over Africa [e.g., *Afiesimama et al.*, 2006; *Sylla et al.*, 2009] and results from sensitivity tests using the domain considered in this study suggested this convection scheme simulated precipitation most accurately (not shown).

[8] The aerosol direct radiative forcing is calculated using the NCAR Community Climate Model (CCM3) radiative package [*Kiehl et al.*, 1996], in which three aerosol optical properties are specified: extinction coefficient, single scattering albedo, and asymmetry parameters. These optical parameters are dependent on aerosol physical parameters, solar wavelength, and the environmental relative humidity, variables calculated by the model [*Solmon et al.*, 2006, 2008]. Only the direct and semidirect aerosol radiative effects are calculated, since there is no aerosol-microphysics coupling in the current version of RegCM3. This is, however, not an unrealistic assumption for southern Africa during the dry season, since *Swap et al.* [2003] suggested that relative humidity and precipitation are so low in the austral winter

that the indirect effects are essentially of little consequence, and the subcontinent is influenced by aerosols largely through direct radiative forcing only.

[9] Both black carbon (BC) and organic carbon (OC) are assumed to be primary aerosols, directly emitted into the atmosphere in hydrophobic and hydrophilic forms. Aging from the hydrophobic to the hydrophilic form occurs at a pseudo-first-order rate of $7.1 \times 10^{-6}\ \mathrm{s}^{-1}$ [*Cooke and Wilson*, 1996]. Both hydrophobic and hydrophilic forms of BC and OC are vertically mixed by convective clouds using the same vertical weighting factor as sulfate following *Tan et al.* [2002]. Wet deposition of the hydrophilic species occurs via large-scale and convective precipitation [*Giorgi and Chameides*, 1986]. Dry deposition velocities for the hydrophilic components are assumed to be $0.2\ \mathrm{cm\ s}^{-1}$ over water and $0.025\ \mathrm{m\ s}^{-1}$ land, while for the hydrophobic form it is assumed to be $0.025\ \mathrm{m\ s}^{-1}$ over all surfaces [*Huang et al.*, 2007]. Wavelength-dependent optical properties are prescribed for both BC and OC and external mixing is assumed for both species. A more detailed description of this simple aerosol scheme can be found in the works of *Solmon et al.* [2006] and *Huang et al.* [2007].

[10] RegCM3 also contains an online dust scheme which calculates emission, transport, and deposition of four particle size bins [*Zakey et al.*, 2006]. The emissions scheme is based on the works of *Marticorena and Bergametti* [1995] and *Alfaro and Gomes* [2001]. The only major dust emission sources in the region include small point sources along the west coast of Namibia in the Namib Desert [*Eckardt and Kuring*, 2005], the Makgadigkadi Pan in Botswana, and Etosha Pan in northern Namibia [*Goudie and Wells*, 1995]. Nevertheless, dust sources have been included in all simulations in order to more accurately characterize the regional natural atmospheric aerosol burden.

2.2. Experiment Design

[11] The model domain covers all of southern Africa and adjacent oceanic areas from 18°N to 43°S and from 10°W to 59°E; however, only the region southward of 5°N is discussed. A horizontal grid point spacing of 60 km is used, and the model includes 18 vertical levels extending to 25 mb. Although a resolution of 60 km is fairly coarse (RCMs can presently run down to ~10 km resolution), the purpose of this study is to provide a first-degree quantitative estimate of the aerosol radiative impacts over the region during the main biomass burning season. To this extent, a large domain size, as well as several years of simulation, was decided best to accomplish these goals.

[12] A 6 year period from 1 January 2001 to 31 December 2006 is analyzed (simulations were started from 1 April 2000, but the first 9 months were considered spin-up period). NCEP-DOE-II Reanalysis data [*Kanamitsu et al.*, 2002] are used for initial and boundary conditions, while NOAA OISST weekly averages [*Reynolds et al.*, 2002] are used as sea surface temperature (SST) forcing. It is important to note at this point that, since RegCM3 is an atmosphere-only model, in standard configuration there is no aerosol radiative feedback on SSTs and surface fluxes over the ocean (however, simulations to test sensitivity to an instantaneous SST feedback were carried out to explore this further, see section 4.4).

[13] Inflow/outflow boundary conditions are used; thus, no aerosol is advected into the domain from outside, but aerosol can freely advect out when they reach the domain boundaries and flow is outward. These assumptions neglect the contribution of external sources to the regional aerosol budget; however, since we are concerned mainly with the impact of southern African biomass burning aerosol, the impact of aerosol from other regions, can for the purposes of this study, be ignored. Also, winds generally tend to blow out of the domain region, northward along the western coast, thus aerosol from West Africa, the only other significant aerosol source near the domain boundaries, is not likely to be circulated into the domain during the austral winter season.

[14] Model simulated aerosol radiative effects are evaluated using two four-member ensembles. The first set of simulations (CTRL) include aerosols but take no account of their radiative interactions, while the second set of simulations (AERO) uses the same initial and boundary forcings and includes the aerosol radiative forcing. The four members of each ensemble were initiated from consecutive days, 1–4 April 2000. A study by *Giorgi and Bi* [2000] investigating the internal model variability of RegCM3 found that there was little sensitivity to the magnitude or source of the perturbation. They tested and compared the difference between simulations carried out with continuous perturbation of the lateral boundary conditions and simulations where only the initial conditions were perturbed and found no significant difference in model error between the two experiments. It was thus considered that starting simulations on consecutive days (effectively varying initial conditions only) was sufficient to initiate internal model variability.

[15] In order to estimate the random internal model error, the variability between averaged surface shortwave (SW) forcing for the region where aerosol optical depth (AOD) > 0.3 was calculated. This was found to vary between $0.25\ \mathrm{W/m^2}$ within the CTRL ensemble and $1.81\ \mathrm{W/m^2}$ within the AERO ensemble, values which are significantly lower than the difference between ensembles ($40.39\ \mathrm{W/m^2}$). Our analysis focuses on the comparison of these two ensembles in order to isolate the direct and semidirect aerosol radiative forcing on the southern African climate, with particular emphasis on the austral winter season from June to September, when biomass burning peaks in the region.

[16] Since RegCM3 is an atmosphere-only model, the sea surface temperatures (SSTs) are prescribed and there is no aerosol feedback on the SSTs. In order to test the model sensitivity to this factor, a third ensemble of four simulations was carried out using a relatively simple adjustment of SST according to aerosol optical depth (AOD; cf. section 4.4).

2.3. Emission Sources

[17] A high spatial and temporal resolution emission database for BC and OC is used to describe the regional carbonaceous aerosol source. This inventory was constructed using the SPOT-vegetation L3JRC burnt area product [*Tansey et al.*, 2008], has a spatial resolution of 0.5° × 0.5°, covers the period 2000–2007, and is able to capture the daily and interannual variability of emissions [*Liousse et al.*, 2010]. It has particularly been used in the context of the AMMA project. Following *Cooke et al.* [1999], 80% of BC is assumed to be emitted in the hydrophobic form, while 50% of OC is assumed to be hydrophobic upon release. In

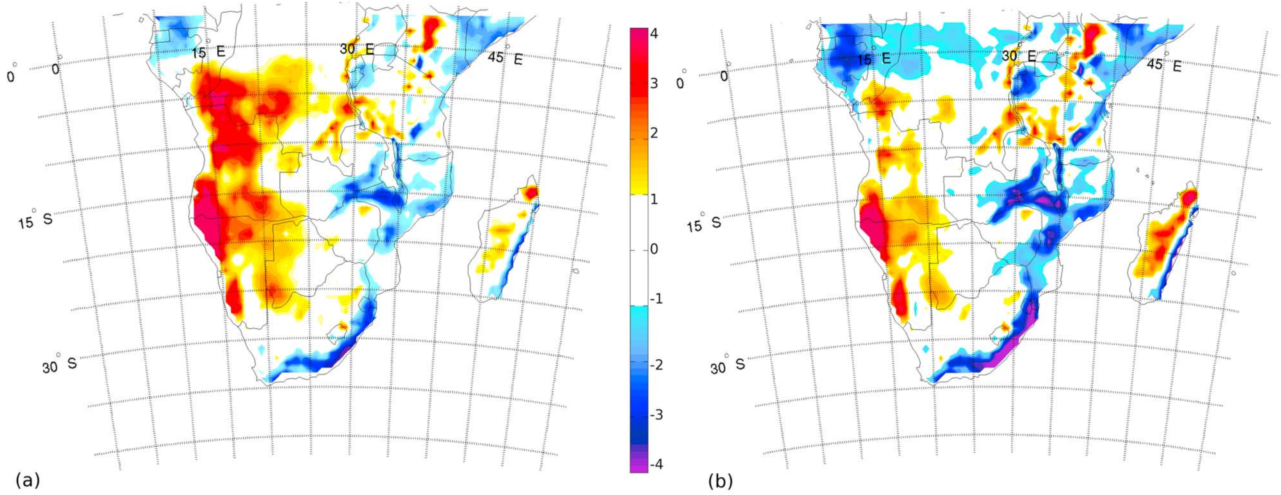

Figure 1. JJAS temperature bias for (a) the control simulation (CTRL) and (b) the aerosol experiment (AERO) compared to the CRU observations (in °C).

terms of dust emissions, four bin sizes are used (0.01–1.00 μm, 1.00–2.50 μm, 2.50–5.00 μm, 5.00–20.00 μm).

[18] A single simulation using the GFEDv2 [*Van der Werf et al.*, 2006] biomass burning emissions inventory was also run for the same period, with the same model parameters. This inventory has been widely used in the literature [e.g., *Myhre et al.*, 2008; *Meyer et al.*, 2008; *Gloudemans et al.*, 2006; *Jain*, 2007], and this sensitivity test was carried out in order to compare and explore the differences in simulated climatic impacts as a result of uncertainty in emissions inventories (which is currently estimated to be up to a factor of 2) [*Korontzi et al.*, 2004]. The GFEDv2 data set consists of global, monthly average BC and OC emissions at 0.5° resolution for the period 1997–2005, calculated based on burned area data from the TRMM-VIRS and ATSR (prior to 2001) and MODIS (post 2001) satellite products [*Van der Werf et al.*, 2006]. Since GFEDv2 emissions don't exist for the final year of simulation (2006), data for 2005 were substituted for this year.

3. Model Validation and Sensitivity Tests

[19] In order to have confidence in the simulated estimates of direct aerosol radiative forcing, it is essential that the model simulates the basic state of the atmosphere and aerosol properties accurately. The following sections discuss validation of the model compared to various observational data sets.

3.1. Surface Air Temperature

[20] Model surface air temperature is compared to the CRU observational data set, developed by the Climate Research Unit at the University of East Anglia [*Mitchell et al.*, 2004]. This data set consists of monthly average surface air temperature over land, gridded at 0.5° × 0.5° resolution and covers the period 1900–2002. Since the simulated period extends from 2001 to 2006, it is only possible to compare the initial two years of model output (2001–2002). Relatively few observations are available for certain regions of southern Africa, most notably Angola and the Democratic Republic of Congo, and the CRU monthly mean temperature is only expected to be accurate to within approximately 1°C [*Jacob et al.*, 2007], with the data set tending toward the climatology particularly in areas where observations are sparse [*Mitchell et al.*, 2004].

[21] For the austral winter season, June to September (JJAS), the model appears to simulate surface temperature relatively well. The control (CTRL) ensemble average bias is shown in Figure 1a. It is clear there is a tendency to overestimate temperature over the western half of southern Africa, west of approximately 30°E, while east of this meridian, temperature tends to be underestimated by a similar magnitude (approximately 1–3°C). Temperature bias may be a result of one or a combination of a number of factors, including cloud cover, precipitation, surface properties (such as surface albedo), energy fluxes, and temperature advection [e.g., *Christensen et al.*, 1997; *Giorgi et al.*, 1998; *Tadross et al.*, 2006]. However, since different factors may play different roles in each region, it is difficult to unambiguously determine the cause of the temperature bias.

[22] The inclusion of the aerosol forcing decreases the simulated temperature bias significantly (Figure 1b), with a large decrease in the positive bias over the western half of southern Africa and only a slight increase of the cold bias over the eastern half of the region. The significance of these results will be discussed further in section 4. It is important to note that typical values of RCM seasonal surface temperature bias range within ±2°C [e.g., *Giorgi et al.*, 1998; *Hudson and Jones*, 2002; *Tadross et al.*, 2006]; thus, our simulation biases fall well within the range of results from other state-of-the-art regional models.

3.2. Precipitation and Circulation

[23] The accurate representation of precipitation is of vital importance, particularly for the wet deposition of aerosols. Simulated precipitation is compared to two data sets: the enhanced CPC Merged Analysis of Precipitation (CMAP) data set [*Xie and Arkin*, 1997] as well as the TRMM 3B43

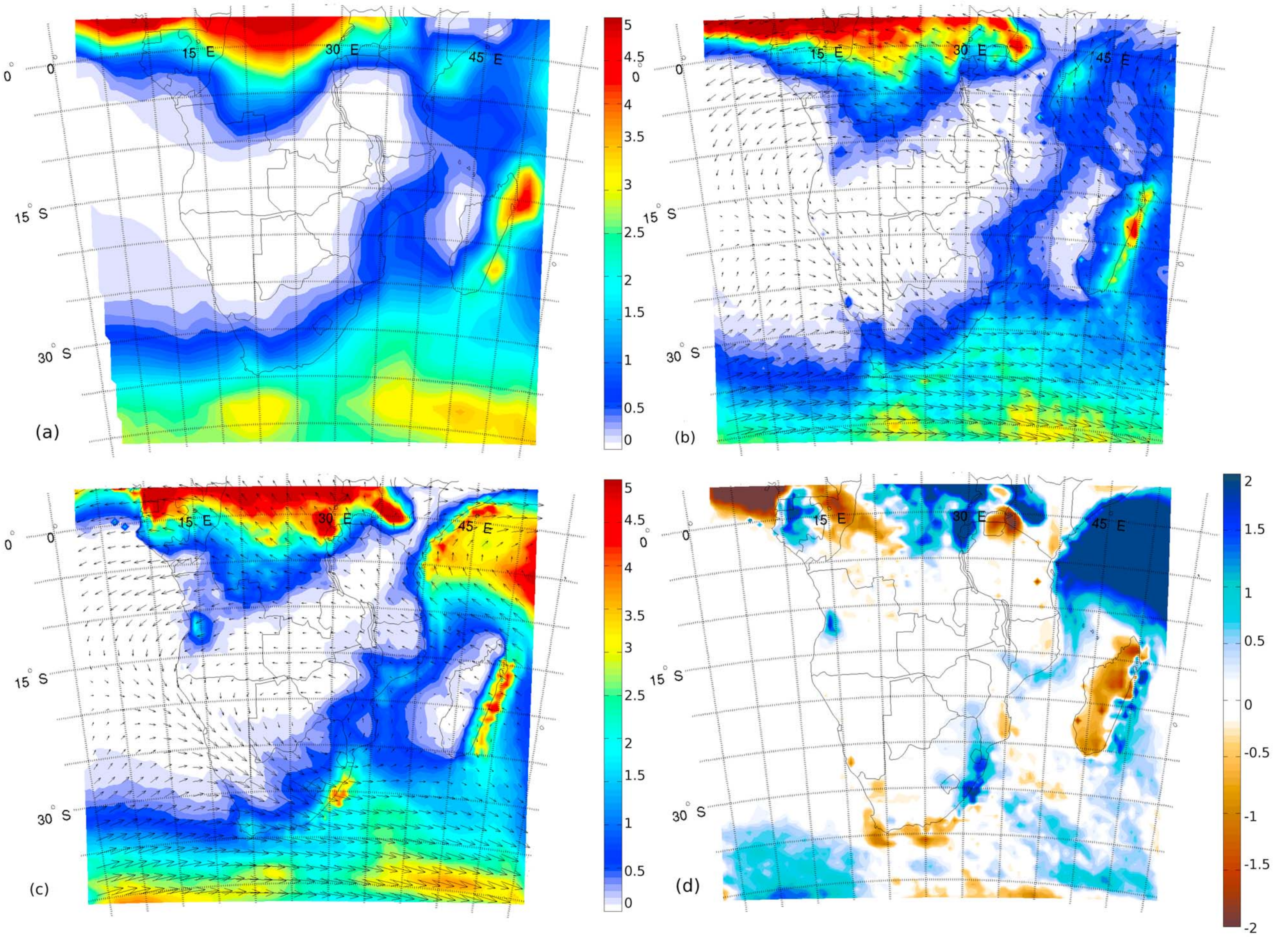

Figure 2. JJAS precipitation climatology (in mm/d), for (a) CMAP, (b) TRMM with NCEP-II 700 hPa winds, (c) RegCM3 with 700 hPa winds, and (d) JJAS precipitation bias (RegCM3-TRMM).

data set [*Adler et al.*, 2000], both of which cover the entire period of simulation, 2001–2006. The enhanced CMAP data set is constructed using precipitation estimates from five satellites (GPI, OPI, SSM/I scattering, SSM/I emission, and MSU), which are then blended with values from the NCEP/NCAR Reanalysis data set, and has a resolution of 1° × 1°. The TRMM 3B43 product is constructed using a combination of TRMM satellite-retrievals adjusted with data from two other ground-based sources (the global gridded rain gauge data from CAMS, produced by the Climate Prediction Center, and the global rain gauge product produced by the Global Precipitation Climatology Center (GPCC)). TRMM data are at 0.25° × 0.25° resolution extending from 50°N to 50°S (covering the entire model domain).

[24] JJAS precipitation is well simulated over most of the southern African domain. Compared to both the CMAP (Figure 2a) and TRMM (Figure 2b) observations, both the magnitude and spatial distribution of simulated precipitation (Figure 2c) is very consistent. The model bias compared to TRMM is shown in Figure 2d. The largest region of overestimated precipitation occurs over the northwest Indian Ocean, off the coast of Kenya and Somalia, where precipitation is overestimated by up to 3 mm/d. A similar positive bias was found by *Davis et al.* [2009] in a study of the East African region, also using RegCM3. It is likely that the model does not accurately simulate the strong dynamics of this monsoonal region. However, since this region does not strongly influence the climate of more southern regions, nor is there a high aerosol load over this area, the precipitation overestimate is likely of little consequence to the aerosol-climate interactions over the subcontinent during the austral winter season.

[25] Perhaps of more importance is the small region of positive bias just southeast of the South African Drakensberg mountain range (situated near ~30°S, 30°E). The complex topography of this small region (up to 3000 m) likely results in the overestimation of orographic rainfall in this area. This feature is common to regional models [e.g., *Christensen et al.*, 1997; *Joubert and Kohler*, 1996; *Afiesimama et al.*, 2006] and is possibly a result of the choice of convective scheme. Since this area lies directly in one of the main exit pathways of aerosol-laden air from the subcontinent [*Tyson et al.*, 1996], the overestimation of precipitation may possibly result in an overestimation of wet aerosol deposition in this region. Compared to TRMM, simulated precipitation is also overestimated by up to 4 mm/d over parts of the equatorial region (between 10°E–15°E and 20°E–35°E), again possibly resulting in an overestimation of wet deposition in

this region. Simultaneously, precipitation is underestimated by a similar magnitude over the equatorial oceanic region between 0–5°N and 0–10°E. Again, these biases are likely the result of the choice of convective scheme, which is particularly sensitive in the equatorial regions.

[26] Since the first absolutely stable layer over much of the interior of the subcontinent preferentially forms at approximately 700 hPa [*Tyson et al.*, 1996] and the moisture flux is maximum at this level [*Freiman and Tyson*, 2000], the NCEP-II and CTRL ensemble JJAS average 700 hPa winds are also included in Figures 2b and 2c, respectively. Overall, the simulated winds show a similar pattern to the NCEP-II reanalysis, both in terms of magnitude and direction. The main features of anticyclonic circulation over the subcontinent south of 10°S are well captured, as is the region of easterly outflow to the Atlantic Ocean between 5°S and 15°S. Likewise, the strong north westerlies and continental outflow from 20°S–35°S, part of the anticyclonic flow system, are also well simulated, as are the strong westerlies between 30°S and 40°S. The monsoonal flux over the Indian Ocean east of Tanzania (5°S–10°S, 30°E–40°E) exhibits slightly too strong an onshore mean flow, while the cross-equatorial winds between 5°S and 5°N also have too much of a northerly component. These features again suggest that the model has difficulty in simulating the monsoon dynamics of this region.

3.3. Aerosol Optical Properties

3.3.1. Aerosol Optical Depth

[27] Simulated aerosol optical depth (AOD) is compared to the two southern African AERONET sites [*Holben et al.*, 1998] for which long-term AOD measurements are available. Figures 3a and 3b show the monthly average model simulated AOD, as well as observations from AERONET [*Holben et al.*, 1998] and the MODIS [*Remer et al.*, 2005] and MISR [*Diner et al.*, 1998] satellite products, for Mongu, Zambia (15.5°S, 23.1°E) and for Skukuza, South Africa (25.0°S, 31.6°E), respectively.

[28] The magnitude of AOD is relatively well simulated at both AERONET sites, with the model capturing the seasonal and interannual variability of AOD quite adequately. Two main issues are, however, apparent at both sites. First, the model simulated AOD clearly peaks 1–2 months prior to both the ground-based AERONET and satellite observations from MODIS and MISR. At Mongu, a site situated near the main biomass burning source regions, observed AOD peaks in September for most years from 2001 to 2006 (2003 is the only exception with AOD peaking in October according to AERONET, MODIS and MISR). RegCM3, however, consistently shows peak AOD in August (with the exception of 2002, when maximum AOD occurs in July). A similar feature is evident at Skukuza, with the model AOD peaking in either July or August, while the ground-based AERONET and satellite observations generally suggest a later peak in September or October. It is important to note that there is more variability in the observed peak AOD at Skukuza than at Mongu, with AERONET, MODIS, and MISR differing for some years by 1 month.

[29] The second discrepancy between simulated and observed AOD occurs outside of the main biomass burning season (November to May), when modeled AOD is significantly underestimated. This feature is particularly evident at Skukuza, where there is less intraseasonal variability in observed AOD than at Mongu. This is largely related to the fact that Skukuza is influenced by the main industrial Highveld region in South Africa, a large source of aerosol emissions that fluctuates little throughout the year [*Piketh et al.*, 1999a].

[30] Simulated aerosol optical depth (AOD) is also compared to the MODIS-terra version 5 daily AOD product [*Remer et al.*, 2005] for the JJAS period. Figure 4 shows the daily composite averages for 2001–2006 for each of the four months from June through September, for MODIS (left column), RegCM3 with AMMA emissions (middle column, emissions contoured over), and the RegCM3-GFED sensitivity test (right column, again with emissions contoured over). The model AOD is screened using the satellite observations, taking the average simulated AOD only for the regions and days for which MODIS observations were available. White areas indicate regions where MODIS daily AOD was not measured (either because of continuous cloud cover or high surface albedo).

[31] The same two features are noticeable in Figure 4: again the RegCM3 simulated AOD appears to peak too early in the season, reaching a maximum in July rather than in August, as the MODIS observations would suggest. And also, by September, there is little significant AOD signal in the simulations, while MODIS observations indicate that the burning season continues well into September and high AOD is maintained during this month, particularly over the Atlantic Ocean. This feature is independent of the emissions inventory used, with both the simulations using the AMMA inventory (from here on the AERO experiment) and that using the GFEDv2 inventory (the GFED experiment) showing the same early AOD peak bias. Although the AERO and GFED simulations show a similar spatial distribution of AOD, there is a significant difference in the magnitude of simulated AOD, with the GFED simulations significantly underestimating the magnitude of observed AOD throughout the biomass burning season. This is a result of the lower emissions (see contours, right column, Figure 4) from the GFEDv2 inventory. Importantly, the timing of peak AOD is also not improved in the GFED simulation, with AOD similarly peaking in July, rather than in August, as the MODIS observations suggest. Differences between the AERO, GFED and CTRL simulations averaged over the oceanic region between 3°N–25°S and 0°–15°E are shown in Table 1. These results indicate that the lower aerosol loading in the GFED simulation resulted in an aerosol-induced surface radiative forcing of only approximately half of that of the AERO simulation (12.83 W/m^2, or 56.37% greater than the AERO simulation). The lower surface radiative forcing resulted in similarly lower 2m temperature, PBL height, and precipitation anomalies. Although results in Table 1 are only averaged over the main Atlantic Ocean outflow region, results for the whole domain were similar in magnitude (not shown).

[32] The relatively large discrepancy in simulated AOD between emissions inventories is likely due, at least in large part, to the different methods used to construct each. The usage of different satellite products, emissions factors and vegetation maps may lead to significant differences in the magnitude, and to a lesser degree, the spatial and temporal location of emissions [*Liousse et al.*, 2010]. A comparison

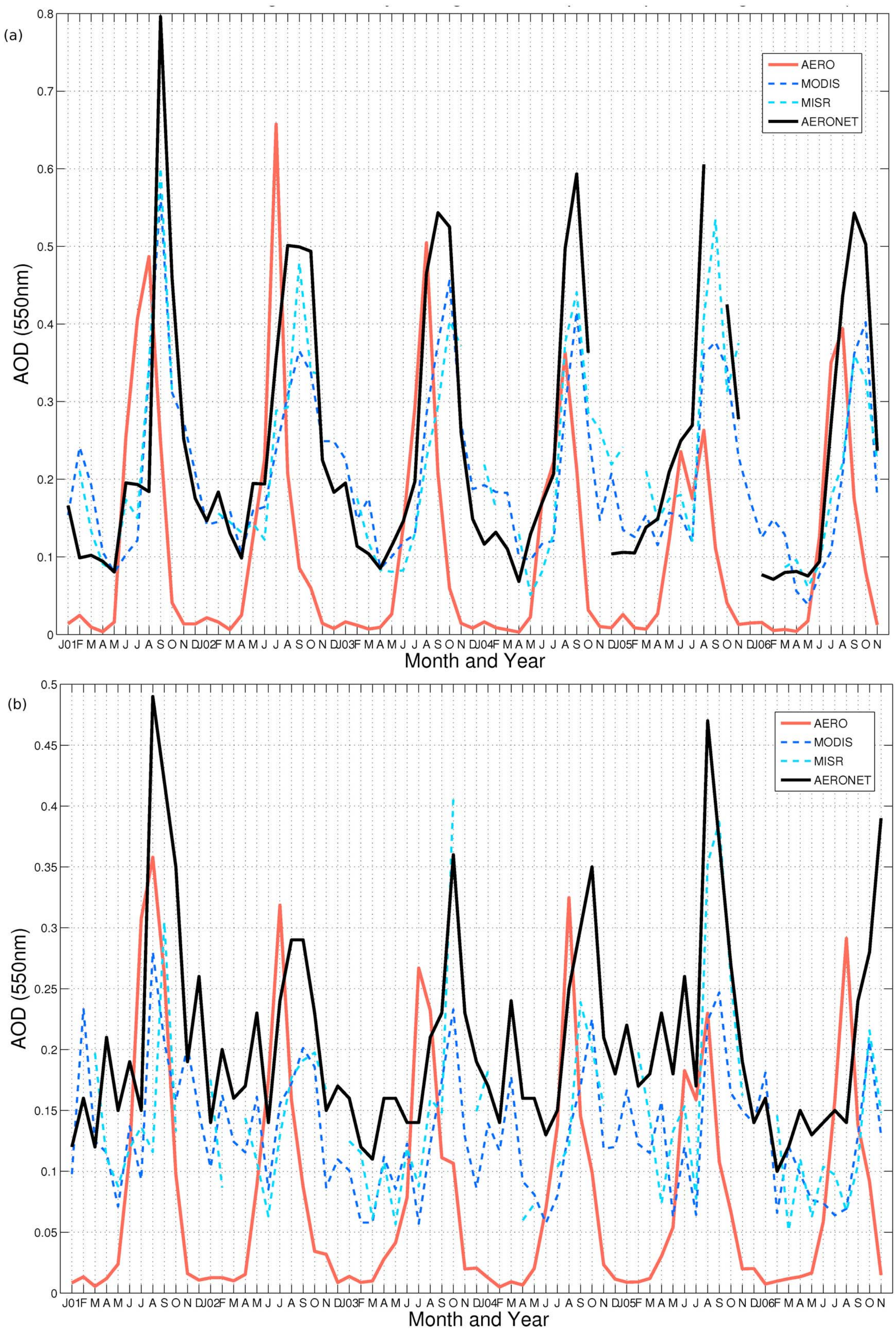

Figure 3. Monthly average aerosol optical depth (AOD) at (a) Mongu, Zambia and (b) Skukuza, South Africa for RegCM3 (aerosol experiment), AERONET, MODIS, and MISR from January 2001 to November 2006.

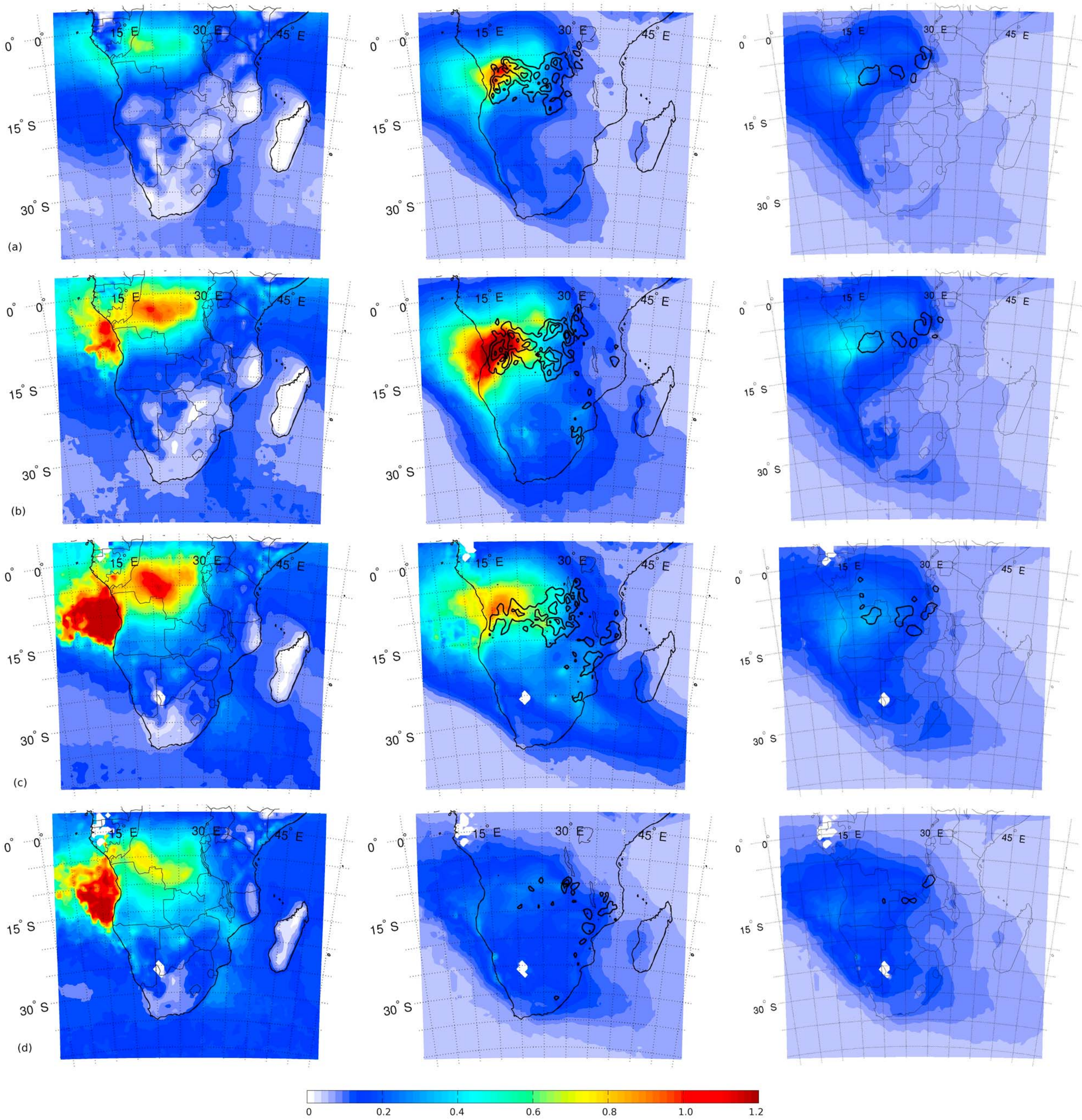

Figure 4. Daily composite aerosol optical depth (AOD) for (a) June, (b) July, (c) August, and (d) September. (left) MODIS, (middle) RegCM3 using AMMA emissions (AERO experiment), and (right) RegCM3 using GFED emissions (GFED experiment). Biomass burning emissions are contoured over the RegCM3 AOD fields (contours every 20 from 0 to 120 mg/m^2/d) for both the middle (AMMA) and right (GFED) columns.

study of CO emissions over Africa [*Barret et al.*, 2010] showed a significantly better correlation between the Liousse et al. (submitted manuscript, 2009) inventory and data from the MOZAIC campaign, than the GFEDv2 inventory [*Van der Werf et al.*, 2006].

[33] Another feature evident in Figure 4 is that the simulated AOD maximum over land is situated approximately 5° too far south in comparison to MODIS. Over the ocean, where satellite observations are perhaps most accurate [*Chu et al.*, 2002; *Remer et al.*, 2002], AOD fields appear to agree better, at least in terms of spatial distribution, with maximum AOD observed between 5°S and 15°S for both RegCM3 and MODIS. It is again clear, however, that the simulated AOD over the ocean reaches a maximum too early in the season.

[34] The disparity between the observed and simulated AOD fields is likely the result of a combination of factors. First, there is large variability in the magnitude and temporal

Table 1. Difference Between the Experiments and Control Ensemble Averaged Over the Atlantic Ocean Region (3°N-25°S, 0°-15°S)[a]

	GFED	AERO	SST
2m Temperature (°C)	−0.07 (−0.36%)	−0.21 (−1.00%)	−0.40 (−1.91%)
PBL Height (m)	−6.07 (−0.89%)	−33.59 (−4.92%)	−43.71 (−6.40%)
Precipitation (mm/d)	+0.08 (+20.08%)	+0.15 (+38.37%)	+0.17 (+41.82%)
Surface RF (W/m^2)[b]	+12.83 (+56.37%)	/	−0.01 (−0.06%)
TOA RF (W/m^2)[b]	+1.44 (+41.05%)	/	−0.06 (−1.63%)

[a] The following tests, GFEDv2 emissions (GFED), the sea surface temperature adjustment (SST), and the ensemble using AMMA emissions (AERO), all were compared with the control (CTRL) ensemble mean (the percentage difference is shown in parentheses).

[b] The surface and top-of-atmosphere (TOA) radiative forcing (RF) are compared to the AERO ensemble rather than the CTRL.

distribution of biomass burning aerosol emissions between different inventories [e.g., *Korontzi et al.*, 2004]. These products are produced using different satellite products (either burnt area and/or hot spot), different emission factors as well as different land surface cover maps. The resulting uncertainty very likely contributes a large part to the error in the timing of simulated AOD field and possibly influences the position of the simulated AOD, which is collocated with the region of maximum emission during all months (see Figure 4, middle and right columns).

[35] Second, the simulated low-level winds (surface to 850 hPa), important for aerosol transport from the source regions, appear to be too weak between 5°N–15°S and 15°E–30°E (not shown). The NCEP reanalysis suggests that on average, southwesterly winds of up to 3 m/s prevail over the continent in this region. RegCM3, however, simulates winds that come rather from the west, and which are generally weaker (~2 m/s) in this area. Northward aerosol transport is thus likely underestimated in the model and may contribute to the underestimation of AOD compared to the MODIS product between 0° and 5°S. Dynamically, the tropical region is difficult to simulate accurately and tracer transport is also strongly influenced by convection. We cannot exclude model deficiencies in horizontal and convective transport which can affect the distribution of AOD. For example the vertical aerosol transport, linked to convection, can be too weak, and thus too little aerosol is transported into the middle troposphere and further northward in the model.

[36] Third, much of the main biomass burning region is covered by savanna, a surface challenging to remote sensing as a result of the discontinuous canopy structure and associated crown shadowing [*Privette and Roy*, 2005]. A study by *Hao et al.* [2005], for example, indicated that MODIS AOD measurements over Zambia were up to 40%–50% lower in cases of high AOD, compared to handheld sun photometers. It was hypothesized that this underestimation was possibly a result of the surface albedo and land surface properties used in the retrieval algorithm, as well as the instrument look angle. This error may at least partly account for the significant difference between observed and simulated AOD over the savanna regions between 5°S and 15°S.

[37] Finally, the simulations carried out do not include biogenic, industrial, or sea-salt aerosol, and thus, AOD is likely to be underestimated, particularly outside of the biomass burning season, when these other aerosol sources dominate the regional atmospheric loading [*Maenhaut et al.*, 1996; *Piketh et al.*, 1999a; *Tyson and Gatebe*, 2001]. This is most likely why monthly average AOD outside of the main biomass burning season is underestimated compared to observations, as previously noted (see Figure 3).

3.3.2. Single Scattering Albedo

[38] The single scattering albedo (SSA) is a vital parameter determining the absorptive properties of the aerosol. Numerous SSA observations of the regional aerosol have been collected during the various field experiments in the southern African region. *Leahy et al.* [2007] suggest, from in situ and AERONET observations, that a value of 0.85 ± 0.02 is representative for southern Africa during the biomass burning season. Observations over the Atlantic Ocean, off the coast of Namibia and Angola indicate higher values, with an average of 0.93 ± 0.06, likely because the aerosol measured in this case was well aged and possibly mixed with sea salt [*Formenti et al.*, 2003]. Similarly, observations over Etosha, Namibia, by *Haywood et al.* [2003] indicate values of 0.89 ± 0.01. RegCM3 simulated bulk SSA values fall within the range 0.83–0.95, well within the observed range over southern Africa, and follow the pattern suggested by observations (low SSA near biomass burning sources with young aerosol and higher SSA for aged aerosol further from source regions; not shown). The model thus appears capable of simulating realistic aerosol optical properties over southern Africa, lending confidence to results of the radiative forcing calculations discussed in section 4.

[39] To date, very few regional climate modeling studies considering the aerosol-climate interaction over southern African have been carried out. Thus, although the temporal and spatial distribution of simulated AOD could certainly be improved, the model simulation of meteorological variables and aerosol properties is considered sufficient as a first step toward estimating the potential impacts of the direct and semidirect aerosol radiative effects on the southern African climate.

4. Simulated Aerosol Impacts

[40] This section evaluates the direct and semidirect effects of the simulated aerosol fields by comparing the average of both AERO and CTRL ensembles for the JJAS period from 2001 to 2006. Results from the two sensitivity tests (GFED and SST) are also discussed.

4.1. Radiative Forcing

[41] Clear-sky surface, top-of-atmosphere (TOA), and atmospheric radiative forcing due to aerosols in the AERO experiment are shown in Figures 5a, 5b, and 5c, respectively. The surface radiative forcing is strongly negative and mirrors the AOD field, with maximum surface radiative forcing up to −60 W/m^2 occurring under the region of maximum AOD (see contours on Figure 5c). Simulated values compare well with those obtained during the SAFARI-2000 campaign. For

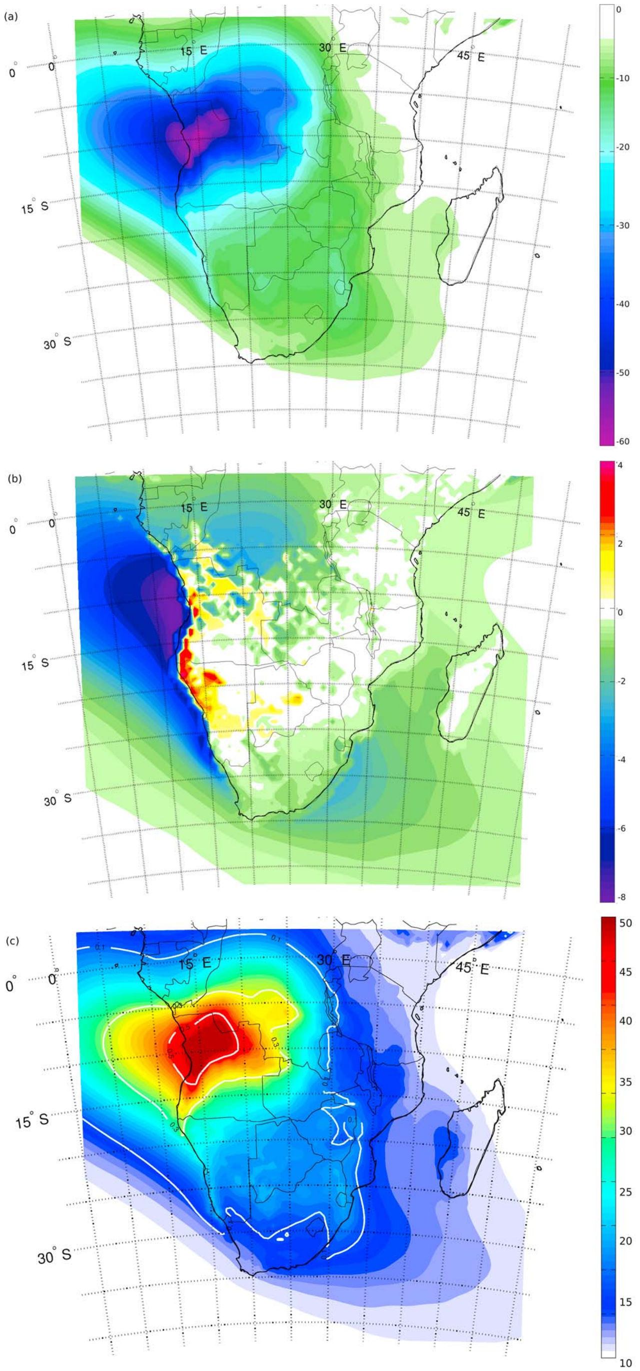

Figure 5. JJAS average clear-sky (a) surface, (b) top-of-atmosphere (TOA), and (c) atmospheric radiative forcing attributable to aerosols (in W/m^2).

example, *Campbell et al.* [2003] calculated a surface flux forcing of −50 W/m^2 using lidar measurements over Skukuza, in South Africa, during a smoke haze event in September 2000. Similarly, *Bergstrom et al.* [2003] estimated values ranging between −57 and −200 W/m^2 at Inhaca Island, off the coast of Mozambique during a number of high AOD events in August and September 2000. Using a radiative transfer model in combination with GCM-simulated and MODIS-observed aerosol fields, *Abel et al.* [2005] estimated that monthly average surface radiative forcing ranged between −5.9 and −56.7 W/m^2 for September. Also using RegCM3, *Zhang et al.* [2008] showed that an AOD of up to 0.6 resulted in a negative surface forcing of greater than −35 W/m^2 over the Amazon biomass burning region. Thus, the surface radiative forcing simulated in this study appears to fall well within the range of simulated and observed values for the southern African region and for biomass burning regions in general.

[42] The clear-sky surface radiative forcing (Figure 5a) is negative over nearly the entire southern African subcontinent, suggesting that despite biomass burning being mostly limited to the savanna regions, the impacts of aerosol on the surface radiative balance are observed throughout the region as a result of the extensive recirculation and transport that occurs. The two main exit pathways of aerosol-laden air, to the Atlantic and Indian Oceans, are also clearly visible, the latter having a weaker surface radiative signal, likely since the model simulates less aerosol transport in the Indian Ocean plume. It is also possible, however, that the surface radiative forcing signal is weaker because of simulated wet and dry deposition that occurs during transport from the main biomass burning regions further north.

[43] The decreased surface radiative forcing results in decreased surface temperatures, as exhibited by a decreased positive temperature bias over much of the western half of southern Africa (compare Figures 1a and 1b, as described above). This is a direct result of aerosol absorption and scattering decreasing incoming shortwave radiation reaching the surface. Similar positive temperature biases have been found in previous RCM studies over southern Africa, and it was hypothesized that this was likely due to overestimated incoming solar radiation at the surface [e.g., *Tadross et al.*, 2006]. Thus, the inclusion of the aerosol direct radiative effect appears, at least in our case, to improve the simulation of surface temperature, and likely most surface processes, over much of southern Africa.

[44] The clear-sky TOA shortwave radiative forcing indicates whether there is a cooling or warming of the surface-troposphere system. It is strongly related to aerosol and surface properties [*Liao and Seinfeld*, 1998], and thus, over land regions the TOA signal varies to a large extent due to the variable underlying vegetation types, as shown by the spatial variability exhibited over land in Figure 5b. Where absorbing aerosol are simulated over desert, semidesert, and short grass-covered regions, where surface albedo is relatively high, the planetary albedo is reduced, and the clear-sky TOA forcing is positive, indicating an overall warming radiative tendency of the surface-troposphere column. Such a region is clearly evident in a narrow band along the west coast from 10°S–25°S, where a high aerosol load over a high albedo surface results in a positive TOA forcing of up to 4 W/m^2. Over darker, lower albedo surfaces such as forest (covering the region between 5°S and 5°N) and over the adjacent oceans, the clear-sky TOA forcing is negative, indicating an average radiative cooling tendency of the surface-troposphere column. Negative clear-sky TOA forcing is maximum over the Atlantic Ocean, where it reaches up to −8 W/m^2. It is important to note, that it is clear-sky TOA radiative forcing that is considered in this case. In fact, the presence of low-level stratocumulus clouds in the marine boundary layer below an elevated aerosol layer likely results

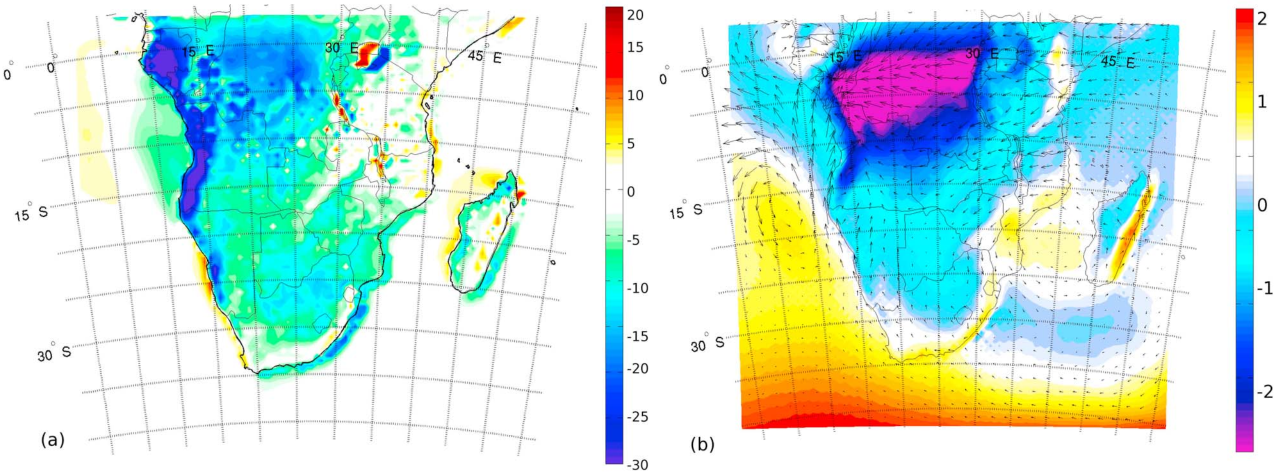

Figure 6. JJAS anomaly (aerosol-control experiment) (a) planetary boundary layer height (percentage change) and (b) 700 hPa anomaly winds (wind intensity is indicated by the size of the arrows, while cool (warm) colors indicate a decrease (increase) of the modulus of the wind).

in a positive whole-sky TOA forcing over much of this region [*Keil and Haywood*, 2003; *Magi et al.*, 2003; *Schmid et al.*, 2003; *Abel et al.*, 2005]. A semipermanent stratocumulus cloud sheet exists off the coast of Namibia and Angola and is present for much of the biomass burning season [*Abel et al.*, 2005]. The aerosol loading therefore potentially has a significant positive TOA forcing in this region, which cannot be diagnosed by the clear-sky TOA forcing. Unfortunately, at present, no diagnostic exists in RegCM3 to visualize the simulated whole-sky TOA forcing due only to aerosols (i.e., excluding the radiative contribution due to clouds), so we are unable to assess the model's performance of this feature compared to observations.

[45] Figure 5c shows the atmospheric radiative forcing attributable to aerosols (i.e., the difference between the TOA and surface forcing), where positive forcing indicates heating of the atmosphere. It is clear that the highly absorbing biomass burning aerosol result in considerable atmospheric diabatic heating over much of southern Africa, particularly over the main biomass burning region (up to 50 W/m^2). The distribution of atmospheric heating clearly mirrors both the surface radiative forcing pattern (Figure 5a) as well as the JJAS average AOD signal (contours Figure 5c). The full implications of this heating are further discussed in sections 4.3 and 4.4.

4.2. Surface Energy Balance

[46] The large negative surface radiative forcing decreases energy available at the surface, partly shutting down surface fluxes and modifying the surface energy budget over much of southern Africa. The sensible heat (SH) flux decreases over almost the entire subcontinent, and is maximum (decreases of up to 50%) in the main biomass burning region (not shown). In contrast, the latent heat (LH) flux change is more variable (also not shown). A region of increased LH flux occurs near the equator (between 5°N and 5°S). In the tropics, where values of potential evaporation are high, changes in soil moisture can have substantial impact on the latent heat flux [*Delworth and Manabe*, 1989]. Since this region receives more precipitation in the AERO simulation (see section 4.3 and Figure 9 below), the soil moisture increases and this likely increases the LH flux. Over the rest of southern Africa there is little change in LH flux due to the predominantly dry conditions.

[47] As a result of the significant decrease in surface turbulent fluxes over much of the subcontinent, the average planetary boundary layer (PBL) height decreases. Figure 6a shows the JJAS average percentage change in PBL height due to aerosols, which clearly decreases over much of the subcontinent. The decrease is largest, up to 30%, along the west coast of the subcontinent between 0° and 15°S, while decreases of approximately 15% occur over much of the main biomass burning region. Small regions of increased PBL height occur over the large East African lakes (Lakes Malawi, Tanganyika and Victoria) as well as off the west coasts of Madagascar, South Africa, and southern Namibia. The regions of increased PBL height are likely linked to dynamical feedbacks and precipitation anomalies, which are further discussed in section 4.4.

[48] Figure 6b shows the change in sea level pressure (SLP) due to aerosols. SLP decreases in a similar fashion to the PBL height (compare Figures 6a and 6b), since the reduced surface radiative forcing also results in decreased surface pressure. The 1000 hPa anomaly winds are also shown in Figure 6b and clearly show that surface convergence occurs in the main biomass burning region (5°N–10°S, 10°E–30°E). Again, this is the result of reduced surface fluxes and surface cooling in this region. Anomalous cyclonic circulation is induced both over the Atlantic Ocean (between ~10°S–25°S and 0°–10°E) and over the Mozambican channel in the Indian Ocean (between ~10°S–30°S and 25°–50°E). These are the two main aerosol outflow pathways and the relatively high AOD in these regions result in lower surface pressures and anomalous cyclonic motion at the surface.

4.3. Effect of the Aerosol Loading on Mean Regional Dynamics

[49] Changes in the surface energy budget as well as atmospheric diabatic heating induced by aerosols are likely to change atmospheric stability, circulation patterns, as well as

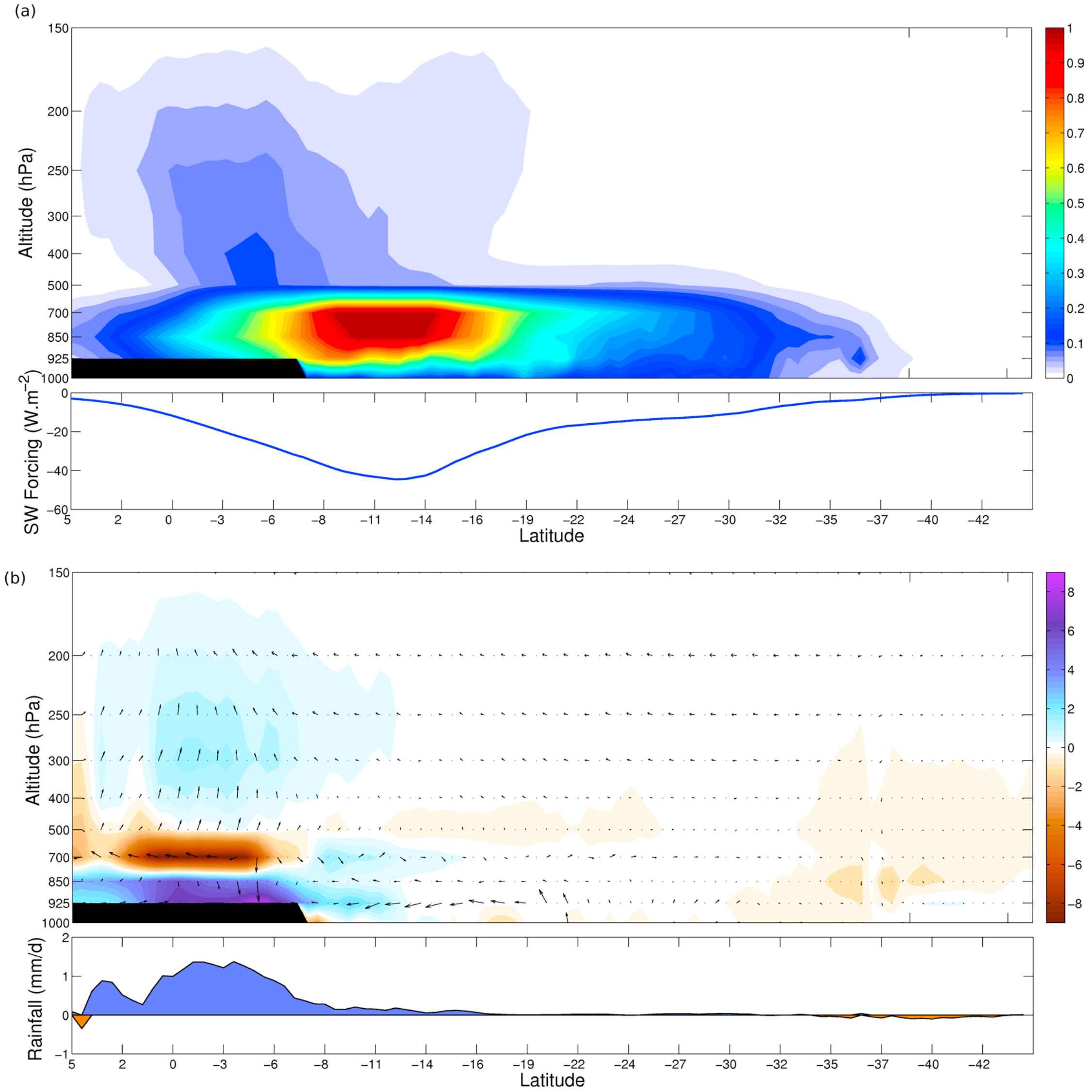

Figure 7. JJAS latitudinal profiles of (a) heating rate anomaly (aerosol-control experiment) in °C/d (vertical profile, top) and surface radiative forcing in W/m^2 (bottom) and (b) (cloud liquid water path (CLWP) anomaly (in mg/kg, vertical profile, top) and precipitation anomaly (bottom) averaged over 12°E–25°E. Only points above the land surface are taken into account in the averages.

cloud and precipitation distribution [e.g., *Dubovik et al.*, 2000; *Kaufman et al.*, 2002; *Takemura et al.*, 2002; *Lau et al.*, 2006]. Figure 7a shows the meridional vertical cross section of the aerosol-induced change (difference between AERO-CTRL ensemble averages) in atmospheric SW heating as well as surface radiative forcing (inset below) averaged over 12°E–25°E. This SW heating rate difference includes all feedbacks (i.e., from clouds as well as from aerosol); however, the main signal appears to be largely due to aerosol forcing since it is very much consistent with the distribution of aerosol concentrations (not shown).

[50] Maximum aerosol-induced heating (up to 1°C/d) and surface forcing (up to −48 W/m^2) occurs over the main source region, centered near 12°S. Two characteristic regions emerge: one situated between the equator and approximately 12°S, where there is a vertical extension of aerosol diabatic heating as a result of enhanced convective aerosol transport; and a second region south of 12°S, where the aerosol layer is clearly trapped below approximately 500 hPa and where diabatic heating is largely confined below this level. The simulated aerosol trapping in this region indicates that the model appears to accurately simulate the 500 hPa absolutely stable layer, which is a very important, semipermanent feature of the southern African atmosphere during the winter season [*Tyson et al.*, 1996].

[51] The simulated heating rate values appear to fall well within (and perhaps even below) the range of observed values over the southern African continent. For example, *Keil and Haywood* [2003] calculated values of similar magnitude (1.77°C/d) using a radiative transfer model and observations of aerosol and cloud properties from SAFARI-2000, while instantaneous heating rates of up to 4°C/d over Mongu, in

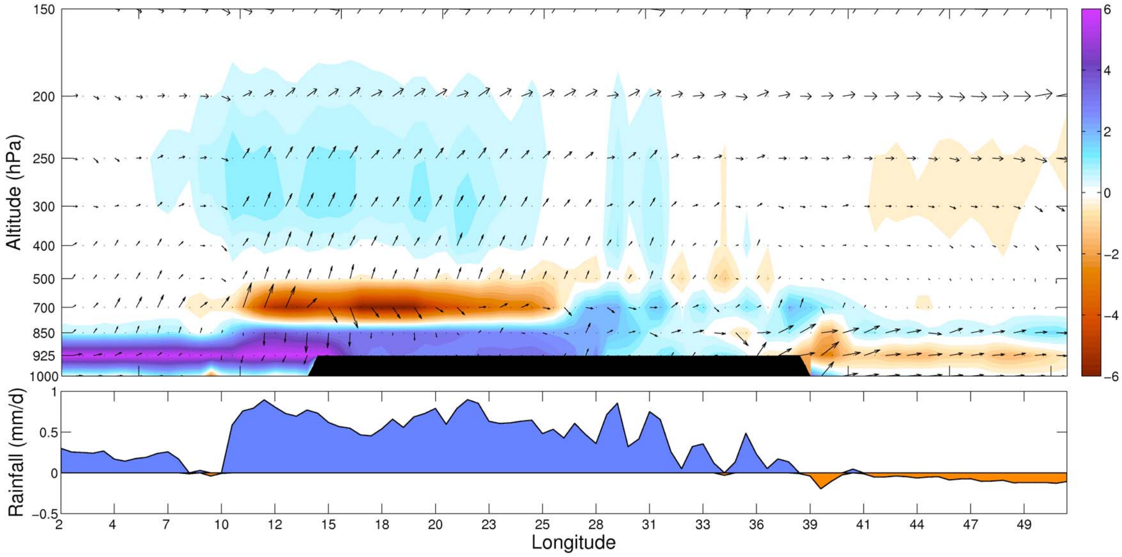

Figure 8. JJAS longitudinal cloud liquid water path (CLWP) anomaly (aerosol-control experiment) (in mg/kg, vertical profile, top) and precipitation anomaly (bottom), averaged over 0°S–15°S latitude. Only points above the land surface are taken into account in the averages.

Zambia and 1.5°C/d over Inhaca Island, Mozambique were measured by *Pilewskie et al.* [2003].

[52] Figure 7b shows the meridional average vertical circulation (again the difference between AERO-CTRL ensemble means) cloud liquid water path (CLWP) and precipitation anomalies (inset below) averaged over the same region (12°E–25°E). The distinction between the two regions discussed above is even clearer. In the convective region, north of approximately 8°S, CLWP significantly increases throughout much of the atmosphere. This increase is associated with a clear increase in upward vertical velocity above 700 hPa and results in a positive precipitation anomaly. The diabatic warming in the aerosol layer is sufficient to induce initial uplift, which further amplifies deep convection. The triggering of convection by aerosol is, however, only evident in the tropical rain belt, where atmospheric conditions are favorable to instability.

[53] Figure 8 shows a zonal vertical cross-section of CLWP, wind and precipitation anomalies (differences AERO-CTRL ensemble averages), averaged over 5°N–10°S. It clearly illustrates a Walker-like circulation branch induced by the aerosol load and convection anomaly, similar to the "elevated heat pump" effect described by *Lau et al.* [2006, 2009]. In the lower troposphere, below 700 hPa, subsidence is enhanced as a result of the strong surface radiative cooling and decrease in surface fluxes that occurs in the main biomass burning region. Similar results were found by *Solmon et al.* [2008] for dust aerosol over West Africa, where aerosol-induced surface cooling and flux reduction were similarly observed. They found that this was generally a drying mechanism if taken alone. In our case, however, the competing heat pump effect, which increases convective precipitation, is dominant because of the strongly absorbing nature of biomass burning aerosols compared to that of dust.

[54] In the northeastern part of the domain (Figure 8) small negative CLWP and precipitation anomalies are observed. This relative drying is associated with slight subsidence, corresponding to the descending branch of the Walker-like circulation anomaly (between 23°E and 49°E in Figure 8), which is triggered by the atmospheric aerosol burden. A decrease of the mean 700 hPa wind intensity is also observed (Figure 6b, ~5°N–15°S, 35°E–50°E), which likely results in decreased onshore moisture flux from the warm ocean, and thus a reduction in CLWP in this region.

[55] Over the ocean, between 2°E and 10°E (see Figure 8) where SST's are prescribed and the surface does not cool in response to the aerosol forcing (in standard model configuration), only aerosol diabatic heating occurs and uplift is induced in the lower troposphere, increasing low-level moisture in this region. The extent and intensity of induced uplift is, however, vertically limited compared to over land, as a result of the more stable nature of the atmosphere over this part of the ocean [*Tyson and Preston-Whyte*, 2000]. It is acknowledged that the present model setup does not account for SST reduction as a result of the negative aerosol surface radiative forcing.

4.4. Sensitivity to an Aerosol-Induced SST Adjustment

[56] Current estimates of the impact of aerosol AOD on SST are variable and depend on the oceanic region studied [e.g., *Evan*, 2007; *Lau and Kim*, 2007; *Foltz and McPhaden*, 2008]. In order to investigate this aspect further, an ensemble of simulations were run artificially decreasing SST as a function of AOD (0.8°C/unit AOD). This value was established from studies where mixed layer ocean models were used to simulate the impact of decreased radiative fluxes on SST in the dust Atlantic outflow [cf. *Yoshioka et al.*, 2007; *Martinez Avellaneda*, 2010; *Evan*, 2007]. These estimates vary as a result of the mixed layer depth used, as well as to some degree depending on the observations and or model used; however, a value of 0.8°C/unit AOD seemed a reasonable compromise for this sensitivity test.

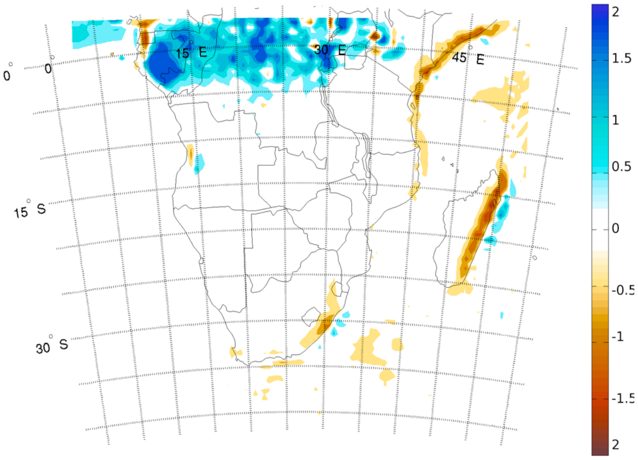

Figure 9. JJAS precipitation anomaly (aerosol-control experiment) in mm/d.

[57] The simulated aerosol feedback on SSTs was found to have only a small impact on the simulated continental surface temperature, radiative feedbacks, and precipitation signals compared to the original AERO ensemble. Differences between the AERO and SST and the CTRL ensemble means (AERO-CTRL and SST-CTRL) averaged over the region 3°N–25°S, 0°–15°E, where AOD is high over the Atlantic Ocean, are shown in Table 1. Although 2m temperature decreases are slightly greater in the SST ensemble (which is as expected since the sea surface cools as a result of the AOD) than for the AERO ensemble, this appears to have little impact on simulated precipitation (SST ensemble precipitation increasing by +0.17 mm/d compared to +0.15 mm/d in the AERO ensemble). The dynamical response induced by the ocean surface cooling and reduction of oceanic surface fluxes leads locally to stabilization and a possible reduction of moisture advection from the sea to the continent. However, this anomaly does not appear, in our case, to be large enough to out-compete those linked to aerosol-induced changes in diabatic heating and increased convection, which are largest over the continent. We acknowledge again that a fully coupled mixed layer ocean-atmosphere-aerosol model would be necessary to more realistically simulate and explore the seasonal modification of SST by the aerosols.

4.5. Aerosol Effects on the African Easterly Jet

[58] The enhancement of deep convection over land, as discussed above, is associated with an enhancement of easterly circulation at approximately 700 hPa, as seen in the anomaly circulation in Figure 8. Near 5°S, this 700 hPa easterly circulation (shown in Figure 2) is associated with the southerly branch of the African Easterly Jet (AEJ-S), which, as documented by *Nicholson and Grist* [2003], is especially active during August and September. The AEJ-S forms as a result of the thermal and energy gradient between the tropical and subtropical savanna regions further south and the active phase of the AEJ-S is related to enhanced precipitation in the convective belt [*Nicholson and Grist*, 2003]. A similar pattern is shown in the anomaly induced by biomass burning aerosols in our case (see Figure 7b, near 5°S). It appears that the regional aerosol loading during the biomass burning season (1) affects the surface temperature gradient through reduced incident solar radiation and (2) increases instability and induces precipitation over the southern edge of the rain belt. This latter mechanism efficiently cools the surface in the rain belt, thus strengthening and shifting the thermal gradient maximum further south. The consequence of this is a strengthening and southward shift of the AEJ-S as observed in Figure 7b. A similar enhancement of the northerly branch of the African Easterly Jet (AEJ-N) was also noted by *Lau et al.* [2009] and *Miller et al.* [2010] during outbreaks of Saharan dust over West Africa. The strengthening and shift of the AEJ-N was also found to be associated with a northward shift and increase in West African monsoonal precipitation [*Lau et al.*, 2009]. These patterns depend on the absorbing nature of the aerosol, the more absorbing the aerosol, and the more intense the feature [*Solmon et al.*, 2008]. The high concentrations of absorbing biomass burning aerosol in this study render a pattern consistent with the effects induced by absorbing aerosol over other regions [e.g., *Lau et al.*, 2009; *Solmon et al.*, 2008]. Incidentally, the enhancement of the AEJ-S is likely to impact interhemispheric transport of biomass burning products from the Southern Hemisphere, as documented by *Mari et al.* [2008].

4.6. Effect of the Aerosol Loading on Regional Precipitation

[59] Figure 9 shows the JJAS average precipitation difference (AERO-CTRL). The increase in precipitation induced by the elevated heat pump effect between 5°N and 5°S is clear, as is the small decrease in precipitation over the northwest Indian Ocean. The increase in precipitation in the equatorial region is in the range of 10%–50% (compared to the CTRL simulation) and improves the negative bias over land observed between ~14°E and 20°E. The positive bias in the rest of the equatorial region is, however, increased. The decrease over the northwest Indian Ocean is of a similar magnitude, also up to 50% compared to the CTRL ensemble mean, but in this region the negative anomaly reduces the positive bias observed in the CTRL (see Figure 2d). Over the southern part of the domain, south of approximately 5°S little change in precipitation is observed. This is not surprising as little or no precipitation occurs south of approximately 8°S during the austral winter season (see Figure 2). The only exceptions are weak decreases in precipitation in narrow bands along the eastern coastal regions of South Africa (between ~30°S–35°S and ~20°E–40°E), Madagascar (~15°S–25°S, ~45°E–50°E), and Tanzania, Kenya, and Somalia (~5°N–15°S, ~40°E–50°E). This tropospheric drying anomaly is likely associated with a positive surface pressure anomaly over land and decreased onshore moisture flux in the eastern part of the domain as described above, both of which likely lead to the simulated decrease in precipitation.

[60] Despite a very low average precipitation signal in the southern part of the domain, it was noted that much stronger precipitation signals over the southwest of the domain (between ~25°S–35°S and 25°E–40°E) were associated with days where aerosol-laden air exited the subcontinent to the southwest Indian Ocean. These so-called "outflow events" were observed during SAFARI-2000 and termed the "river of smoke" [*Annegarn et al.*, 2002]. In the following section, we study the simulated aerosol impact on regional precipitation

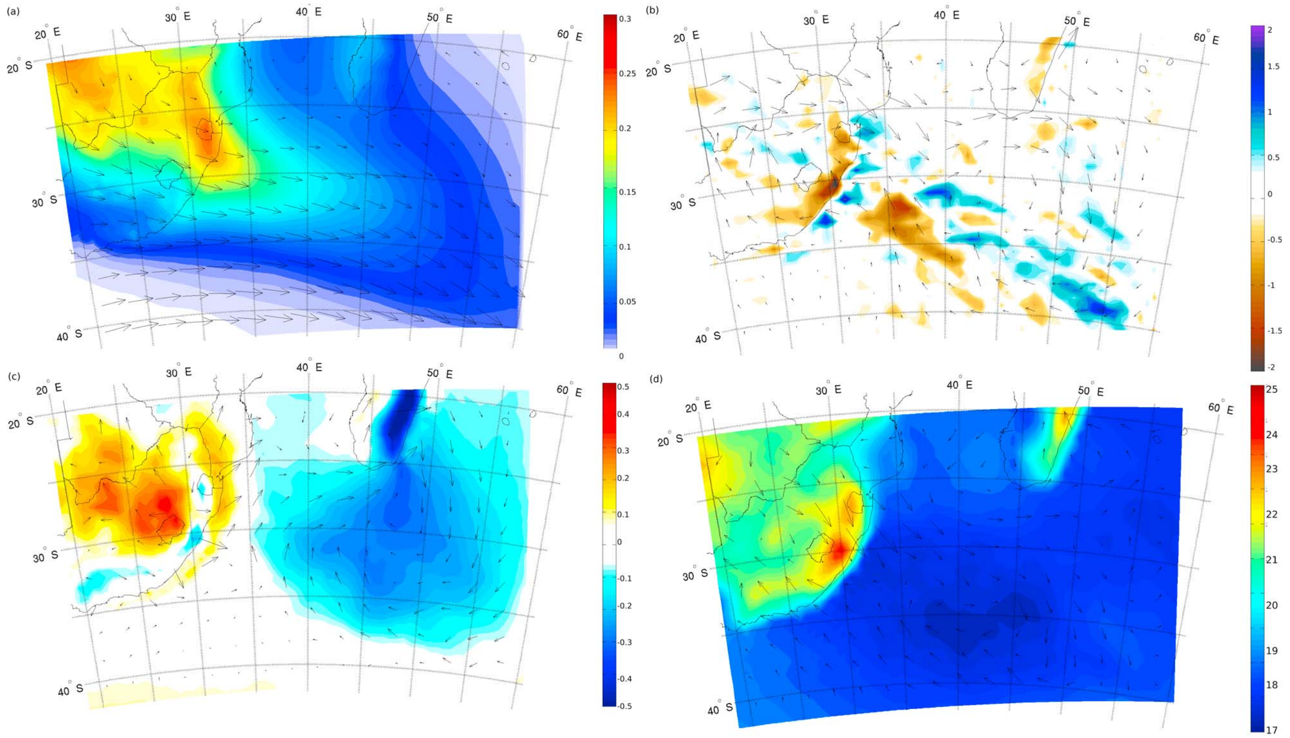

Figure 10. (a) Average aerosol optical depth (AOD) and control (CTRL) 700 hPa winds, (b) 500 hPa geopotential height anomaly (in m) and 500 hPa wind anomaly (aerosol-control experiment), (c) sea level pressure height anomaly (in m) and 1000 hPa wind anomaly, and (d) aerosol-induced change in precipitation (mm/d) and 700 hPa wind anomaly. Plots a–d averaged for all outflow events.

during these "extreme AOD" outflow events (rather than the seasonal mean climate response, as described above).

4.7. Impact of Aerosols During Indian Ocean Outflow Events

4.7.1. Self-Organizing Maps (SOMs)

[61] In order to select days when aerosol outflow events were simulated by the model, a self-organizing map (SOM) [*Kohonen*, 1995] was used. A SOM classifies the input data into a predefined number of reference patterns or modes using an unsupervised artificial neural network. The patterns produced are essentially generalized states, but the given number of states is fully representative of the input data. Although the technique is relatively new to the field of climatology, it has been used successfully in a number of studies [e.g., *Crane and Hewitson*, 1998; *Cavazos*, 2000; *Reusch et al.*, 2005a]. The main advantage of the SOM technique is that it can be applied to nonlinear data (such as the continuum of atmospheric conditions) and it does not force orthogonality (as, for example, in principal component analysis (PCA)). In addition, the results can be directly physically interpreted, unlike, for example, the PCA approach which produces patterns of variance rather than direct physical states of the atmosphere. In an idealized comparison study, *Reusch et al.* [2005b] found that SOMs were more robust, isolated predefined patterns, and attributed variance more accurately than a rotated PCA analysis.

[62] For our purposes, the SOM approach is applied to the daily AOD output for the season under discussion (June through September), for all ensemble members together. It is important to note that this technique is not an "optimal" clustering technique, since clusters of roughly equal size are produced. However, since the SOM approach treats the input data as a continuum, which is more representative of the nature of synoptic conditions which have a large influence on the AOD signal, this technique is considered to be appropriate for our purposes.

4.7.2. Precipitation Changes During Indian Ocean Outflow Events

[63] Aerosols are recirculated over southern Africa until a cold front sweeps over the southern portion of the subcontinent, inducing offshore flow and effectively "cleansing" the atmosphere [*Stein et al.*, 2003] by inducing vertical mixing and aerosol washout through precipitation processes. Aerosol-laden air is essentially drawn south and eastward along the leading edge of these frontal systems and exits the subcontinent to the southwest Indian Ocean.

[64] Selected results from the SOM analysis are shown in Figure 10. These results are the average of all days found to fall into the category of "outflow events." In total 219 (or 7.48%) days out of the 2928 JJAS days (732 days from each of the four ensemble members) were classified as an outflow event. During such events a band of high AOD is clearly visible exiting the subcontinent near ~28°S, 32°E (see Figure 10a), similarly situated to the observed position of the "river of smoke." This outflow of air is associated with offshore flow (wind arrows, Figure 10a) occurring along the leading edge of a low-pressure system. Precipitation occurs

during the passage of these frontal systems, contributing a relatively large proportion of the annual rainfall over the southwestern region of South Africa [*Tyson and Preston-Whyte*, 2000].

[65] The simulated aerosol loading induces a rather consistent banded precipitation anomaly to the south of the main core of the outflow plume (along the leading edge of the front), with precipitation increases of up to 2 mm/d (or approximately 20%) along the southern reaches of the plume but decreases of a similar magnitude directly to the south of the band of increase (see Figure 10b). This precipitation signal appears to be the result of the changes in frontal dynamics as shown by the circulation anomalies at various levels (Figures 10b–10d), which indicate a northward shift of the outflow circulation, consistent with the precipitation signal.

[66] We propose the following mechanisms to explain this signal:

[67] Within the plume, absorbing aerosol locally warms the atmosphere by up to 0.5°C in the main core region near 700 hPa (not shown). This increases the north-south thermal gradient compared to the CTRL simulation and hence increases baroclinic instability in the region. This is compounded by the fact that the aerosol warming induces uplift and anomalous cyclonic circulation throughout the lower atmosphere over the ocean (as described in section 4.3). Sea level pressure is reduced in the region of cyclonic anomaly (Figure 10c), while the 500 hPa geopotential height increases as a result of the aerosol-induced heating at altitude (Figure 10d). The location of the cyclonic circulation anomaly (leaning southward and eastward with height) is a result of the baroclinic nature of the passing frontal system. Anomalous offshore (northwesterly) flow is seen at the surface (Figure 10c), 700 hPa (Figure 10b), and 500 hPa (Figure 10d). We suggest that the increased baroclinicity and cyclonic anomaly effectively sharpen the frontal gradient, thus narrowing the region where precipitation occurs, increasing precipitation in the northern half of the frontal precipitation band and decreasing precipitation in the southern half. The precipitation band itself does not appear to shift significantly northward, it is rather a narrowing of this band that seems to occur.

[68] During outflow events precipitation also decreases along the eastern escarpment region of South Africa (~25°S–32°S, 25°E–32°E). This feature is similar to what occurs on average in the JJAS season (see Figure 9). As described above, anomalous offshore circulation throughout most of the lower troposphere decreases the moisture carried onshore from the warm and moist Indian Ocean, thus reducing the orographic rainfall in this small region (and simultaneously reducing the positive bias in this area; see Figure 2d). There is little precipitation change over the rest of the southern Africa south of 8°S during outflow events (not shown), since only the southern reaches of the subcontinent are affected by the passage of westerly waves and the associated precipitation. More northern regions do not receive precipitation from these systems and climatologically, little precipitation occurs during the austral winter season [*Tyson and Preston-Whyte*, 2000].

[69] In contrast, the circulation changes and precipitation signal on days with no aerosol outflow are weak and inconsistent (not shown). Since no elevated aerosol layer is present, no anomalous atmospheric heating occurs, and as expected, there is little significant change in the circulation patterns or precipitation. Since the frequency of outflow events during JJAS is fairly low, the precipitation signal is not seen in the seasonal average precipitation difference (Figure 9). Rather, the signal from nonoutflow days dominates. As described above, for the JJAS seasonal average, precipitation in fact decreases over much of the region between 20°S–40°S and 20°E–40°E. As described above, this is a result of anomalous cyclonic circulation, which induces decreased onshore (southeasterly) flow, and therefore, less moist air is transported onshore air from the Indian Ocean to this region.

5. Conclusions

[70] The regional climate model RegCM3 has been used to explore the direct and semidirect aerosol radiative effects on southern Africa during the austral dry season (JJAS). Two ensembles of four simulations were run: a control, where no aerosol radiative effects were considered, and the experiment, within which the radiative impacts were calculated. The simulated aerosol burden induced changes of regional surface fluxes and dynamics. The following results are most pertinent:

[71] 1. The regional climatic features of southern Africa during the dry, austral winter were well simulated. Both precipitation and temperature were consistent with observation; with simulated temperature improving compared to the CRU observations when the aerosol radiative forcing was taken into account. AOD was relatively well simulated, with best consistency over the ocean. The simulated maximum over land occurred approximately 5° farther south than the maximum suggested by MODIS AOD observations, and the simulated AOD peaked too early in the biomass burning season compared to AERONET ground-based observations as well as compared to MODIS and MISR observations. Outside of the main biomass burning season AOD was underestimated compared to AERONET, likely because the simulations carried out did not include industrial, biogenic or sea-salt aerosols. A sensitivity test using the GFEDv2 biomass burning inventory showed much lower AOD, and neither the temporal nor spatial disparity in AOD was improved.

[72] 2. A strong decrease in clear-sky surface radiative forcing (up to -60 W/m^2 in the main biomass burning region) resulted in decreased surface turbulent fluxes and reduced surface temperature over the entire southern African subcontinent (again, maximum over the main biomass burning area). The positive temperature bias over the western half of the southern African subcontinent was thus reduced, and in general, the simulation of surface temperature improved.

[73] 3. As a result of the strongly absorptive nature of the simulated biomass burning aerosols, diabatic atmospheric warming occurred. This was maximum, up to 1°C/d, near the 700 hPa level in the main biomass burning aerosol source region.

[74] 4. The simulated surface cooling and heating at altitude stabilized the lower troposphere below the main aerosol layer at 700 hPa. However, in the equatorial regions, stability was reduced above 700 hPa, where an elevated heat pump effect was observed. Aerosol warming increased deep convection between 5°N and 8°S, which in turn resulted in increased precipitation in this region.

[75] 5. Despite significant temperature changes, little precipitation signal is exhibited over the rest of southern Africa. This is expected, since climatologically, stable conditions are predominant and very little or no rainfall occurs over much of the region south of 8°S during JJAS.

[76] 6. The southern branch of the African Easterly circulation (AEJ-S) appears to be enhanced and shifted southward as a result of the simulated aerosol burden. This is likely the result of a combination of two features: the surface temperature gradient is enhanced through the surface dimming effect, and the increased precipitation in the equatorial region further cools the surface in the rain belt, thus strengthening and shifting the thermal maximum further southward.

[77] 7. A similar climatic response was found in the GFED sensitivity test; however, the magnitude of the response was considerably smaller (~50% less in the case of most atmospheric variables). This is largely a result of the lower emissions suggested by the GFEDv2 data set [*Van der Werf*, 2006].

[78] 8. A third ensemble of four members was carried out using a simple adjustment of SST according to the AOD to account for the surface forcing of aerosol over the oceans. The results from these simulations, however, were not significantly different to those without the SST adjustment (AERO ensemble). The sensitivity to the emissions inventory (GFED versus AERO experiment) was considerably larger.

[79] 9. A self-organizing map (SOM) was used to extract days upon which a plume of high AOD occurred over the southwest Indian Ocean. During aerosol outflow events to the Indian Ocean (the "river of smoke" phenomenon), which occur as a result of the passage of a low-pressure system, diabatic warming and induced cyclonic circulation anomalies enhance baroclinicity along the leading edge of the frontal system. The gradient of the front is increased, and as a result, the band of precipitation along the leading edge becomes narrower and more intense. These events only affect precipitation in a small region between ~20°S–40°S and 20°E–40°E. It shows, however, that aerosols affect not only the mean climatic state but can also perturb the statistics of intense dynamical events on a daily scale.

[80] This study should be further complemented by a number of sensitivity tests. The large uncertainty regarding biomass burning emissions inventories and particularly the underestimation of September burning activity will need to be explored. A higher-resolution study on a more specifically aimed domain (e.g., the tropical belt) would also further elucidate the aerosol impacts on the southerly branch of the African Easterly Jet. The possible SST cooling effect, which will require a coupled atmosphere-ocean model, will also need to be investigated. Recently RegCM3 has been coupled to the ROMS ocean model [*Ratham et al.*, 2009], so a study of this nature will also be carried out in future. Also, a new land surface scheme has recently been coupled to RegCM3 [CLM3; *Steiner et al.*, 2009] and will be tested.

[81] Finally, longer simulations will need to be carried out in order to explore the interannual variability of the observed climatic impacts of the regional aerosol burden. It has been suggested that aerosol outflow events are more pronounced and located further northward during La Niña periods than El Niño periods [*Stein et al.*, 2003]. Thus, it is possible that the precipitation signal during outflow events observed in this study varies between La Niña and El Niño periods. A longer simulation period would allow an in-depth investigation of the interannual variability of the aerosol-climate impacts over southern Africa and whether these are significantly different between La Niñas and El Niños.

[82] **Acknowledgments.** This work was funded through a CNRS BDI-PED bursary ("bourse de pays developpant"). We would like to thank the Centre for High Performance Computing (CHPC), Cape Town, for the use of extensive computing facilities. The authors also wish to acknowledge the provision of TRMM, MODIS and MISR data through the GIOVANNI Web interface, the provision of CMAP data from the NOAA/OAR/ESRL PSD, as well as the AERONET team for use of their data. The authors would also like to thank two anonymous reviewers for their helpful suggestions and comments.

References

Abel, S. J., E. J. Highwood, J. M. Haywood, and M. A. Stringer (2005), The direct radiative effect of biomass burning aerosols over southern Africa, *Atmos. Chem. Phys. Discuss.*, *5*, 1165–1211.

Adler, R. F., J. Huffmann, D. T. Bolvin, S. Curtis, and E. J. Nelkin (2000), Tropical rainfall distributions determined using TRMM combined with other satellite rain gauge information, *J. Appl. Meteorol.*, *39*, 2007–2023.

Afiesimama, E. A., J. S. Pal, B. J. Abiodun, W. J. Gutowski Jr., and A. Adedoyin (2006), Simulation of West African monsoon using the RegCM3: Part 1. Model validation and interannual variability, *Theor. Appl. Clim.*, *86*, 23–37.

Alfaro, S. C., and L. Gomes (2001), Modeling mineral aerosol production by wind erosion: Emission intensities and aerosol size distributions in source areas, *J. Geophys. Res.*, *106*(D16), 18,075–18,084, doi:10.1029/2000JD900339.

Alleaume, S., C. Hely, J. Le Roux, S. Koronitzi, R. J. Swap, H. H. Shugar, and C. O. Justice (2005), Using MODIS to evaluate heterogeneity of biomass burning in southern African savannas: A case study in Etosha, *Int. J. Remote Sens.*, *26*, 4219–4237.

Andreae, M. O., and P. Merlet (2001), Emission of trace gases and aerosol from biomass burning, *Global Biogeochem. Cycles*, *15*, 955–966.

Annegarn, H. J., L. Otter, R. J. Swap, and R. J. Scholes (2002), Southern Africa's ecosystem in a test-tube: A perspective on the Southern African Science Initiative (SAFARI 2000), *S. Afr. J. Sci.*, *98*, 111–113.

Barret, P., et al. (2010), Impact of West African Monsoon convective transport and lightning Nox production upon the upper tropospheric composition: A multi-model study, *Atmos. Chem. Phys. Discuss.*, *10*, 5719–5738.

Bergstrom, R. W., T. P. Ackerman, and L. W. Richards (1982), The optical properties of particulate elemental carbon, in *Particulate Carbon: Atmospheric Life Cycle*, edited by G. T. Wolff, and R. L. Klimisch, pp. 43–49, Plenum, New York.

Bergstrom, R. W., P. Pilewskie, B. Schmid, and P. B. Russel (2003), Estimates of the spectral aerosol single scattering albedo and aerosol radiative effects during SAFARI 2000, *J. Geophys. Res.*, *108*(D13), 8474. doi:10.1029/2002JD002435.

Bond, T. N., G. Habib, and R. W. Bergstrom (2006), Limitations in the enhancement of visible light absorption due to mixing state, *J. Geophys. Res.*, *111*, D20211, doi:10.1029/2006JD007315.

Cahoon, D. R., Jr., B. J. Stocks, W. R. Coffer III, and K. P. O'Neill (1992), Seasonal distribution of African savanna fires, *Nature*, *359*, 812–815.

Campbell, J. R., E. J. Welton, J. D. Spinhirne, Q. Ji, S. Tsay, S. J. Piketh, M. Barenbrug, and B. N. Holben (2003), Micropulse lidar observations of tropospheric aerosols over northeastern South Africa during the ARREX and SAFARI 2000 dry season experiments, *J. Geophys. Res.*, *108*(D13), 8497, doi:10.1029/2002JD002563.

Cavazos, T. (2000), Using self-organizing maps to investigate extreme climate events: An application to wintertime precipitation in the Balkans, *J. Clim.*, *13*, 1718–1732.

Christensen, J. H., B. Machenhauer, R. G. Jones, C. Schar, P. M. Ruti, M. Castro, and G. Viscont (1997), Validation of present-day regional climate simulations over Europe: LAM simulations with observed boundary conditions, *Clim. Dyn.*, *13*, 489–506.

Chu, D. A., Y. J. Kaufman, C. Ichoku, L. A. Remer, D. Tanré, and B. N. Holben (2002), Validation of MODIS aerosol optical depth retrieval over land, *Geophys. Res. Lett.*, *29*(12), 8007, doi:10.1029/2001GL013205.

Cooke, W. F., C. Liousse, H. Cachier, and J. Feichter (1999), Construction of a 1° × 1° fossil fuel emission data set for carbonaceous aerosol and implementation and radiative impact in the ECHAM4 model, *J. Geophys. Res.*, *104*(D18), 22,137–22,162, doi:10.1029/1999JD900187.

Cooke, W. F., and J. J. N. Wilson (1996), A global black carbon aerosol model, *J. Geophys. Res.*, *101*(D14), 19,395–19,409, doi:10.1029/96JD00671.

Crane, R. G., and B. C. Hewitson (1998), Doubled CO_2 precipitation changes for the Susquehanna basin: Down-scaling from the GENESIS general circulation model, *Int. J. Climatol.*, *18*, 65–76.

Crutzen, P. J., and M. O. Andreae (1990), Biomass burning in the tropics: Impacts on atmospheric chemistry and biogeochemical cycles, *Science*, *250*, 1669–1678.

Crutzen, P. J., L. E. Heidt, J. P. Krasnec, W. H. Pollock, and W. Seiler (1979), Biomass burning as a source of atmospheric gases CO, H_2, N_2O, NO, CH_3Cl and COS, *Nature*, *282*, 253–256.

Davis, N., J. Bowden, F. Semazzi, and L. Xian (2009), Customization of RegCM3 regional climate model for Eastern Africa and tropical Indian Ocean domain, *J. Clim.*, *22*, 3595–3616.

Delworth, T., and S. Manabe (1989), The influence of soil wetness on near-surface atmospheric variability, *J. Clim.*, *2*, 1447–1462.

Dickinson, R. E., A. Henderson-Sellers, and P. J. Kennedy (1993), Biosphere-Atmosphere Transfer Scheme (BATS) version 1e as coupled to the NCAR Community Climate Model, *Tech. Rep.*, National Center for Atmospheric Research, Boulder, Colorado.

Diner, D. J., et al. (1998), Multi-angle Imaging SpectroRadiometer (MISR) description and experiment overview, *IEEE Trans. Geosci. Remote Sens.*, *36*(4), 1072–1087.

Dubovik, O., A. Smirnov, B. N. Holben, M. D. King, Y. J. Kaufman, T. F. Eck, and I. Slutsker (2000), Accuracy assessments of aerosol optical properties retrieved from Aerosol Robotic Network (AERONET) Sun and sky radiance measurements, *J. Geophys. Res.*, *105*(D8), 9791–9806, doi:10.1029/2000JD900040.

Eck, T. F., et al. (2003), Variability of biomass burning aerosol optical characteristics in southern Africa during the SAFARI 2000 dry season campaign and a comparison of single scattering albedo estimates from radiometric measurements, *J. Geophys. Res. 108*(D13), 8477, doi:10.1029/2002JD002321.

Eckardt, F. D., and N. Kuring (2005), SeaWiFS identifies dust sources in the Namib Desert, *Int. J. Remote Sens.*, *26*, 4159–4167.

Evan, A. T. (2007), Comment on "How nature foiled the 2006 hurricane forecasts," *EOS Trans. AGU*, *88*, 271.

Foltz, G. R., and M. J. McPhaden (2008), Impact of Saharan dust on tropical Norht Atlantic SST, *J. Clim.*, *21*, 5048–5060.

Formenti, P., W. Elbert, W. Maenhaut, J. Haywood, S. Osborne, and M. O. Andreae (2003), Inorganic and carbonaceous aerosol during the Southern African Regional Science Initiative (SAFARI 2000) experiment: Chemical characteristics, physical properties and emission data for smoke from African biomass burning, *J. Geophys. Res.*, *108*(D13), 8488, doi:10.1029/2002JD002408.

Freiman, M. T., and S. J. Piketh (2003), Air transport into and out of the industrial Highveld region of South Africa, *J. Appl. Meteorol.*, *42*, 994–1002.

Freiman, M. T., and P. D. Tyson (2000), The thermodynamic structure of the atmosphere over South Africa: Implications for water vapor transport, *Water S. Afr.*, *26*, 153–158.

Fritsch, J. M., and C. F. Chappell (1980), Numerical prediction of convectively driven mesoscale pressure systems: Part 1. Convective parameterization, *J. Atmos. Sci.*, *37*, 1722–1733.

Garstang, M., W. N. Ellery, T. S. Scholes, M. C. Scholes, R. J. Swap, and P. D. Tyson (1998), The contribution of aerosol- and water-borne nutrients to the functioning of the Okavango Delta, Botswana, *S. Afr. J. Sci.*, *94*, 215–222.

Giorgi, F., and W. L. Chameides (1986), Rainout lifetimes of highly soluble aerosols and gases as inferred from simulations with a general circulation model, *J. Geophys. Res.*, *91*(D13), 14,367–14,376, doi:10.1029/JD091iD13p14367.

Giorgi, F., L. O. Shields, and L. McDaniel (1998), Regional nested model simulations of present day and 2xCO2 climate over the Central Plains of the US, *Clim. Change*, *40*, 457–493.

Giorgi, F., and C. Shields (1999), Tests of precipitation parameterizations available in latest version of NCAR regional climate model (RegCM) over continental United States, *J. Geophys. Res.*, *104*(D6), 6353–6375, doi:10.1029/98JD01164.

Giorgi, F., and X. Bi (2000), A study of internal variability of a regional climate model, *J. Geophys. Res.*, *105*(D24), 29,503–29,521, doi:10.1029/2000JD900269.

Gloudemans, A. M. S., M. C. Krol, J. F. Meirink, A. T. J. de Laat, G. R. van der Werf, H. Schrijver, M. M. P. van den Broek, and I. Aben (2006), Evidence for long-range transport of carbon monoxide in the Southern Hemisphere from SCHIAMACHY observations, *Geophys. Res. Lett.*, *33*, L16807, doi:10.1029/2006GL026804.

Goudie, A. S., and G. L. Wells (1995), The nature, distribution and formation of pans in arid zones, *Earth Sci. Rev.*, *38*, 1–69.

Grell, G. A. (1993), Prognostic evaluation of assumptions used by cumulus parameterizations, *Mon. Weather Rev.*, *121*, 764–787.

Grell, G. A., J. Dudhia, and D. R. Stauffer (1994), A description of the fifth-generation Penn State/NCAR mesoscale model version 5 (MM5), *Tech. Note TN-398+IA*, Tech. Rep., Natl. Cent. for Atmos. Res., Boulder, Colo.

Hansen, J., D. Johnson, A. Lacis, S. Lebedeff, P. Lee, D. Rind, and G. Russel (1981), Climate impact of increasing atmospheric carbon dioxide, *Science*, *213*, 957–966.

Hao, W. M., D. E. Ward, R. A. Susott, R. E. Babbitt, B. L. Nordgren, Y. J. Kaufman, B. N. Holben, and D. M. Giles (2005), Comparison of aerosol optical thickness measurements by MODIS, AERONET sun photometers and Forest Service handheld sunphotometers in southern Africa during the SAFARI 2000 campaign, *Int. J. Remote Sens.*, *26*, 4169–4183.

Haywood, J., P. Francis, O. Dubovik, M. Glew, and B. Holben (2003), Comparison of aerosol size dsitributions, radiative properties and optical depths determined by aircraft observations and Sun photometers during SAFARI 2000, *J. Geophys. Res.*, *108*(D13), 8471, doi:10.1029/2002JD002250.

Helas, G., M. O. Andreae, and O. Meinrat (1995), SA'ARI 94: A preliminary view of results, *J. Afr. J. Sci.*, *91*, 360–362.

Helas, G., and J. J. Pienaar (1996), The influence of vegetation fires on the chemical composition of the atmosphere, *S. Afr. J. Sci.*, *92*, 132–136.

Hobbs, P. V., P. Sinha, R. J. Yokelson, T. J. Christian, D. R. Blake, S. Gao, T. W. Kirchstetter, T. Novakov, and P. Pilewskie (2003), Evolution of gases and particles from a savanna fire in South Africa, *J. Geophys. Res.*, *108*(D13), 8485, doi:10.1029/2002JD002352.

Holben, B. N., et al. (1998), AERONET – A federated instrument network and data archive for aerosol characterization, *Remote Sens. Environ.*, *66*, 1–16.

Holtslag, A. A. M., E. I. F. DeBruijn, and H. L. Pan (1990), A high-resolution air mass transformation model for short-range weather forecasting, *Mon. Weather. Rev.*, *118*, 1561–1575.

Huang, Y., W. L. Chameides, and R. E. Dickinson (2007), Direct and indirect effects of anthropogenic aerosol over East Asia, *J. Geophys. Res.*, *112*, D03212, doi:10.1029/2006JD007114.

Hudson, D. A., and R. Jones (2002), Regional Climate Model simulations of present-day and future climates of southern Africa, Tech. Note 39, Hadley Centre for Climate Prediction and Research, Met. Off. Bracknell, England.

Jacob, D., et al. (2007), An intercomparison of regional climate models for Europe: Model performance in present-day climate, *Clim. Change.*, *81*, 31–52.

Jacobson, M. Z. (2001), Strong radiative heating due to the mixing state of black carbon in atmospheric aerosols, *Nature*, *409*, 695–697.

Jain, A. K. (2007), Global estimation of CO emissions using three sets of satellite data for burned area, *Atmos. Environ.*, *41*, 6931–6940.

Joubert, A. M., and M. O. Kohler (1996), Projected temperature increases over southern Africa due to increasing greenhouse gases and sulphate aerosols, *S. Afr. J. Sci.*, *92*, 524–527.

Kanamitsu, M., W. Ebisuzaki, J. Woollen, S.-K. Yang, J. J. Hnilo, M. Fiorino, and G. L. Potter (2002), NCEP-DOE AMIP-II Reanalysis (R-2), *Bull. Am. Meteorol. Soc.*, 1631–1643, doi:10.1175/BAMS-83-11-1631.

Kaufman, Y. J., D. Tanré, and O. Boucher (2002), A satellite view of aerosols in the climate system, *Nature*, *419*, 215–223.

Keil, A., and J. M. Haywood (2003), Solar radiative forcing by biomass burning aerosol particles during SAFARI 2000: A case study based on measured aerosol and cloud properties, *J. Geophys. Res.*, *108*(D13), 8467, doi:10.1029/2002JD002315.

Kiehl, J. T., J. J. Hack, G. B. Bonan, B. A. Boville, B. P. Briegleb, D. L. Williamson, and P. J. Rasch (1996), Description of the NCAR community climate model (CCM3), NCAR Tech. Note, *NCAR/TN-420+STR*, 152 pp., Natl. Cent. for Atmos. Res., Boulder, Colo.

Kohonen, T. (1995), Self-Organizing maps, in *Springer Series in Information Sciences*, vol. 30, Springer, Berlin.

Korontzi, S., D. P. Roy, C. O. Justice, and D. E. Ward (2004), Modeling and sensitivity analysis of fire emissions in southern Africa during SAFARI 2000, *Remote Sens. Environ.*, *92*, 376–396.

Lau, K. M., M. K. Kim, and K. M. Kim (2006), Asian summer monsoon anomalies induced by aerosol direct forcing: The role of the Tibetan Plateau, *Clim. Dyn.*, *26*, 855–864.

Lau, K. M., and K. M. Kim (2007), Reply to comment on "How nature foiled the 2006 hurricane forecasts," *EOS Trans. AGU*, *88*, 105–107.

Lau, K. M., M. K. Kim, Y. C. Sud, and G. K. Walker (2009), A GCM study of the response of the atmospheric water cycle of West Africa and the Atlantic to Saharan dust radiative forcing, *Ann. Geophys.*, *27*, 4023–4037.

Leahy, L. V., T. L. Anderson, T. F. Eck, and R. W. Bergstrom (2007), A synthesis of single scattering albedo of biomass burning aerosol over southern Africa during SAFARI 2000, *Geophys. Res. Lett.*, *34*, L12814, doi:10.1029/2007GL029697.

Liao, H., and J. H. Seinfeld (1998), Radiative forcing by mineral dust aerosols: Sensitivity to key variables, *J. Geophys. Res.*, *103*(D24), 31,637–31,645, doi:10.1029/1998JD200036.

Lindesay, J. A., M. O. Andreae, J. G. Goldammer, G. Harris, H. J. Annegarn, M. Garsta, R. J. Scholes, and B. W. van Wilgen (1996), International Geosphere-Biosphere Programme/International Global Atmospheric Chemistry SAFARI-92 field experiment: Background and overview, *J. Geophys. Res.*, *101*(D19), 23,521–23,530, doi:10.1029/96JD01512.

Liousse, C., et al. (2004), Deriving global quantitative estimates for spatial and temporal distributions of biomass burning emissions, in *Emissions of Atmospheric Trace Compounds*, edited by C. Granier et al., Kluwer Acad., Netherlands.

Liousse, C., et al. (1996), A global three-dimensional model study of carbonaceous aerosols, *J. Geophys. Res.*, *101*, 19,411–19,432.

Liousse, C., et al. (2010), Western African aerosols modelling with updated biomass burning emission inventories in the frame of the AMMA-IDAF program, *Atmos. Chem. Phys. Discuss.*, *10*, 7347–7382.

Maenhaut, W., I. Salma, J. Cafmeyer, H. J. Annegarn, and M. O. Andreae (1996), Regional atmospheric aerosol composition and sources in the eastern Transvaal, South Africa and impact of biomass burning, *J. Geophys. Res.*, *101*(D19), 23,631–23,650, doi:10.1029/95JD02930.

Magi, B. I., P. V. Hobbs, B. Schmid, and J. Redemann (2003), Vertical profiles of light scattering, light absorption and single scattering albedo during the dry, biomass burning season in southern Africa and comparisons of in situ remote sensing measurements of aerosol optical depths, *J. Geophys. Res.*, *108*(D13), 8504, doi:10.1029/2002JD002361.

Mari, C., G. Cailley, L. Corre, M. Saunois, J. L. Attie, V. Thouret, and A. Stohl (2008), Tracing biomass burning plumes from the Southern Hemisphere during the AMMA 2006 wet season experiment, *Atmos. Chem. Phys.*, *8*, 3951–3961.

Marticorena, B., and G. Bergametti (1995), Modeling the atmospheric dust cycle: Part 1. Design of soil-derived dust emission scheme, *J. Geophys. Res.*, *100*(D8), 16,415–16,430, doi:10.1029/95JD00690.

Martinez Avellaneda, N. (2010), The impact of Saharan dust on the North Atlantic circulation, Ph.D. thesis, 107 pp., Univ. Hamburg, Hamburg.

Martins, J. V., P. Artaxo, C. Liousse, J. S. Reid, P. V. Hobbs, and Y. J. Kaufman (1998), Effects of black carbon content, particle size, and mixing on light absorption by aerosols from biomass burning in Brazil, *J. Geophys. Res.*, *103*(D24), 32,041–32,050, doi:10.1029/98JD02593.

Meyer, C. P., A. K. Luhar, and R. M. Mitchell (2008), Biomass burning emissions over northern Australia constrained by aerosol measurements: 1. Modeling the distribution of hourly emissions, *Atmos. Environ.*, *42*, 1629–1646.

Mikhailov, E. F., S. S. Vlasenko, I. A. Podgorny, V. Ramanathan, and C. E. Corrigan, (2006), Optical properties of soot-water agglomerates: An experimental study, *J. Geophys. Res.*, *111*, D07209, doi:10.1029/2005JD006389.

Mitchell, T. D., T. R. Carter, P. D. Jones, M. Hulme, and M. New (2004), A comprehensive set of high-resolution grids of monthly climate for Europe and the globe: The observed record (1901–2000) and 16 scenarios (2001–2100), Tyndall Centre Working paper 55, Norwich.

Myhre, G., T. L. Berntsen, J. M. Haywood, J. K. Sundet, B. N. Holben, M. Johnsrud, and F. Stordal (2003), Modeling the solar radiative impact of aerosols from biomass burning during the Southern African Regional Science Initiative (SAFARI-2000) experiment, *J. Geophys. Res.*, *108*(D13), 8501, doi:10.1029/2002JD002313.

Myhre, G., et al. (2008), Radiative forcing of the direct aerosol effect using a multi-observation approach, *Atmos. Chem. Phys. Discuss.*, *8*, 12,823–12,886.

Nicholson, S. E., and J. Grist (2003), The seasonal evolution of the atmospheric circulation over West Africa and Equatorial Africa, *J. Clim.*, *16*, 1013–1030.

Pal, J. S., et al. (2007), Regional climate modeling for the developing world: The ICTP RegCM3 and RegCNET, *Bull. Am. Meteorol. Soc.*, *88*, 1395–1409.

Perlwitz, J., and R. L. Miller (2010), Cloud cover increase with increasing aerosol absorptivity: A counterexample to the conventional semi-direct aerosol effect, *J. Geophys. Res.*, *115*, D08203, doi:10.1029/2009JD012637.

Pilewskie, P., J. Pommier, R. Bergstrom, W. Gore, S. Howard, M. Rabbette, B. Schmid, P. V. Hobbs, and S. C. Tsay (2003), Solar spectral radiative forcing during the Southern African Regional Science Initiative, *J. Geophys. Res.*, *108*(D13), 8486, doi:10.1029/2002JD002411.

Piketh, S. J., H. J. Annegarn, and P. D. Tyson (1999a), Lower tropospheric aerosol loadings over South Africa: The relative contribution of aeolian dust, industrial emissions and biomass burning, *J. Geophys. Res.*, *104*(D1), 1597–1607, doi:10.1029/1998JD100014.

Piketh, S. J., R. J. Swap, C. A. Anderson, M. T. Freiman, M. Zunckel, and G. Held (1999b), The Ben MacDhui high altitude trace gas and aerosol transport experiment, *S. Afr. J. Sci.*, *95*, 35–43.

Posfai, M., R. Simonics, J. Li, P. V. Hobbs, and P. R. Buseck (2003), Individual aerosol particles from biomass burning in southern Africa: 1. Compositions and size distributions of carbonaceous particles, *J. Geophys. Res.*, *108*(D13), 8483, doi:10.1029/2002JD002291.

Privette, J. L., and D. P. Roy (2005), Southern Africa as a remote sensing test bed: The SAFARI 2000 Special Issue overview, *Int. J. Remote Sens.*, *26*, 4141–4158.

Ratham, J. V., F. Giorgi, A. Kaginalkar, and S. Cozzini (2009), Simulation of the Indian monsoon using the RegCM3-ROMS regional coupled model, *Clim. Dyn.*, *33*, 119–139.

Remer, L. A., et al. (2002), Validation of the MODIS aerosol retrieval over ocean, *Geophys. Res. Lett.*, *29*(12), 8008, doi:10.1029/2001GL013204.

Remer, L. A., et al. (2005), The MODIS aerosol algorithm, products and validation, *J. Atmos. Sci.*, *62*, 947–973.

Reusch, D. B., R. B. Alley, and B. C. Hewitson (2005a), Towards ice core-based synoptic reconstructions of West Antarctic climate with artificial neural networks, *Int. J. Climatol.*, *25*, 581–610.

Reusch, D. B., R. B. Alley, and B. C. Hewitson (2005b), Relative performance of Self-Organizing Maps and Principal Component Analysis in pattern extraction from synthetic climatological data, *Polar Geogr.*, *29*, 188–212.

Reynolds, R. W., N. A. Rayner, T. M. Smith, D. C. Stokes, and W. Wang, (2002), An improved in situ and satellite SST analysis for climate *J. Clim.*, *15*, 1609–1625.

Schmid, B., et al. (2003), Coordinated airborne, spaceborne and ground-based measurements of massive thick aerosol layers during the dry season in southern Africa, *J. Geophys. Res.*, *108*(D13), 8496, doi:10.1029/2002JD002297.

Scholes, M., and M. O. Andeae (2000), Biogenic and pyrogenic emissions from Africa and their impact on the global atmosphere, *Ambio.*, *29*, 23–29.

Seiler, W., and P. J. Crutzen (1980), Estimates of gross and net fluxes of carbon between the biosphere and the atmosphere from biomass burning, *Clim. Change*, *2*, 207–247.

Solmon, F., F. Giorgi, and C. Liousse, (2006), Aerosol modeling for regional climate studies: Application to anthropogenic particles and evaluation over a European/African domain, *Tellus*, *58B*, 51–72.

Solmon, F., M. Mallet, N. Elguindi, F. Giorgi, A. Zakey, and A. Konaré (2008), Dust aerosol impact on regional precipitation over western Africa: Mechanisms and sensitivity to absorption properties, *Geophys. Res. Lett.*, *35*, L24705, doi:10.1029/2008GL035900.

Stein, D. C., R. J. Swap, S. Greco, S. J. Piketh, S. A. Macko, B. G. Doddridge, T. Elias, and R. T. Bruintjies (2003), Haze layer characterization and associated meteorological controls along the eastern coastal region of southern Africa, *J. Geophys. Res.*, *108*(D13), 8506, doi:10.1029/2002JD003237.

Steiner, A. L., J. S. Pal, S. A. Rauscher, J. L. Bell, N. S. Diffenbaugh, A. Boone, L. C. Sloan, and F. Giorgi (2009), Land surface coupling in regional climate simulations of the West African monsoon, *Clim. Dyn.*, *33*, 869–829.

Swap, R. J., M. Garstang, S. A. Macko, P. D. Tyson, W. Maenhaut, P. Artaxo, P. Kallberg, and R. Talbot (1996), The long-range transport of southern African aerosol to the tropical South Atlantic, *J. Geophys. Res.*, *101*(D19), 23,777–23,791, doi:10.1029/95JD01049.

Swap, R. J., et al. (2002), The Southern African Regional Science Inititatve (SAFARI 2000): Overview of the dry season field campaign, *S. Afr. J. Sci.*, *98*, 125–130.

Swap, R. J., H. J. Annegarn, J. T. Suttles, M. D. King, S. Platnick, J. L. Privette, and R. J. Scholes (2003), Africa burning: A thematic analysis of the Southern African Regional Science Initiative (SAFARI 2000), *J. Geophys. Res.*, *108*(D13), 8465, doi:10.1029/2003JD003747.

Sylla, M. B., E. Coppola, L. Mariotti, F. Giorgi, P.M. Ruti, A. Dell'Aquila, and X. Bi (2009), Multiyear simulation of the African climate using a regional climate model (RegCM3) with the high resolution ERA-interim reanalysis, *Clim. Dyn.*, doi:10.1007/s00382-009-0613-9.

Tadross, M. A., W. J. Gutowski Jr., B. C. Hewitson, C. Jack, and M. New (2006), MM5 simulations of interannual change and the diurnal cycle of southern African regional climate, *Theor. Appl. Climatol.*, *86*, 63–80.

Takemura, T., T. Nakajima, O. Dubovik, B. N. Holben, and S. Kinne (2002), Single-scattering albedo and radiative forcing of various aerosols species with a global three-dimensional model, *J. Clim.*, *15*, 333–352.

Tan, Q., Y. Huang, and W. L. Chameides (2002), Budget and export of anthropogenic Sox from east Asia during continental outflow conditions, *J. Geophys. Res.*, *107*(D13), 4167, doi:10.1029/2001JD000769.

Tansey, K., J. M. Grégroire, P. Defoumy, R. Leigh, J. F. Pekel, E. von Bogaert, and E. Bartholomé (2008), A new, global, multi-annual (2000–2007) burnt area product at 1km resolution, *Geophys. Res. Lett.*, *35*, L01401, doi:10.1029/2007GL031567.

Terblanche, D. E., M. P. Mittermaier, S. J. Piketh, R. T. Bruintjies, and R. P. Burger (2000), The Aerosol Recirculation and Rainfall Experiment (ARREX): An initial study on aerosol-cloud interactions over South Africa, *S. Afr. J. Sci.*, *96*, 15–21.

Torres, O., P. K. Bhartia, J. R. Herman, A. Sinyuk, P. Ginoux, and B. Holben (2002), A long-term record of aerosol optical depth from TOMS observations and comparison to AERONET measurements, *J. Atmos. Sci.*, *59*, 398–413.

Tyson, P. D., M. Garstang, and R. Swap (1996), Large-scale recirculation of air over Southern Africa, *J. Appl. Meteorol.*, *35*, 2218–2236.

Tyson, P. D., and C. K. Gatebe (2001), The atmosphere, aerosols, trace gases and biogeochemical change in southern Africa: A regional integration, *S. Afr. J. Sci.*, *97*, 106–118.

Tyson, P. D., and R. A. Preston-Whyte (2000), *The Weather and Climate of Southern Africa*, Oxford Univ. Press, Cape Town.

Van der Werf, G. R., J. T. Randerson, L. Giglio, G. J. Collatz, P. S. Kasibhatla, and A. F. Arellano Jr. (2006), Interannual variability of global biomass burning emissions from 1997 to 2004, *Atmos. Chem. Phys. Discuss.*, *6*, 3175–3226.

Xie, P., and P. A. Arkin (1997), Global precipitation: A 17-year monthly analysis based on gauge observations, satellite estimates, and numerical model outputs, *Bull. Am. Meteorol. Soc.*, *78*, 2539–2558.

Yoshioka, M., N. M. Mahowald, A. J. Conley, W. D. Collins, D. W. Fillmore, C. S. Zender, and D. B. Coleman (2007), Impact of desert dust radiative forcing on Sahel Precipitation: Relative importance of dust compared to sea surface temperature variations, vegetation changes and greehouse gas warming, *J. Clim.*, *20*, 1445–1467.

Zakey, A., F. Solmon, and F. Girogi (2006), Development and testing of a desert dust module in a regional climate model. *Atmos. Chem. and Phys.*, *6*, 4687–4704.

Zhang, Y., R. Fu, H. Yu, R. E. Dickinson, R. N. Juarez, M. Chin, and H. Wang (2008), A regional climate model study of how biomass burning aerosol impacts land-atmosphere interactions over the Amazon, *J. Geophys. Res.*, *113*, D14S15, doi:10.1029/2007JD009449.

C. Liousse and F. Tummon, Laboratoire d'Aérologie, 14 Ave. Edouard Belin, Toulouse 31400, France. (tumf@aero.obs-mip.fr)

F. Solmon, Abdus Salam International Centre for Theoretical Physics, Strada Costiera 11, 34151 Trieste, Italy.

M. Tadross, Climate Systems Analysis Group, University of Cape Town, Cape Town, South Africa.